



**University of Amsterdam**

GRAVITATION AND ASTROPARTICLE PHYSICS AMSTERDAM  
RESEARCH PROJECT PHYSICS AND ASTRONOMY 5354RPP60Y  
MASTER THESIS RESEARCH

---

**Machine learning analysis of  
Gravitational Wave signals from  
Primordial Black Hole binary  
inspirals with Dark Matter spikes**

---

Author: Francesco Marangio

Student ID: 13285343

First Supervisor: Christoph Weniger (C.Weniger@uva.nl)

Second Supervisor: Gianfranco Bertone (G.Bertone@uva.nl)

January 24th, 2024

# Abstract

The research described in this manuscript is an application of a machine learning algorithm for the parameter estimation of Gravitational Waves (GW) from compact binary inspirals with Dark Matter (DM) spikes. Throughout the project, a specific class of black hole mergers was analyzed, namely Primordial Black Hole (PBH) mergers. This work, using simulated GW data, demonstrates the potential of deep learning algorithms for analyzing data generated with Einstein Telescope design sensitivities and how using such computational tools could contribute to the detection of DM. The research can therefore be considered as a Mock Data Challenge towards the GW community. The obtained results show that the proposed deep learning algorithm can be confidently applied to Einstein Telescope simulated data, therefore representing a valuable alternative to classical methods of GW signal detection. Ideas for improving the current deep learning algorithm and the quality of the simulations that have been suggested for investigation in future research.

**Keywords:** Deep Learning, Gravitational Wave, Mock Data Challenge, Einstein Telescope, Dark Matter, Primordial Black Hole

# Contents

<b>1</b>	<b>Introduction</b>	<b>1</b>
1.1	Dark matter detection . . . . .	1
1.2	Gravitational waves in vacuum . . . . .	1
1.2.1	Compact Binaries Inspiral Gravitational Waves . . . . .	2
1.3	Primordial Black Holes . . . . .	3
1.4	Gravitational waves with environmental effects . . . . .	4
1.4.1	Dark matter spikes . . . . .	4
1.4.2	Gravitational atom . . . . .	6
1.4.3	Accretion disks . . . . .	7
1.5	First and second generation detectors . . . . .	8
1.6	Future Gravitational Wave detectors . . . . .	8
1.7	Matched Filtering formalism . . . . .	10
1.8	Bayesian Inference . . . . .	12
1.9	Machine Learning . . . . .	12
1.9.1	Neural Networks . . . . .	13
1.9.2	CNN architecture . . . . .	15
1.10	Regression Analysis . . . . .	17
1.11	Project aims . . . . .	18
<b>2</b>	<b>Methods</b>	<b>18</b>
<b>3</b>	<b>Results</b>	<b>25</b>
3.1	Dataset 1 . . . . .	25
3.2	Dataset 2 . . . . .	29
<b>4</b>	<b>Discussion</b>	<b>32</b>
<b>5</b>	<b>Conclusion</b>	<b>34</b>

# 1 Introduction

## 1.1 Dark matter detection

According to the Lambda-Cold Dark Matter ( $\Lambda$ -CDM) model, cold DM and dark energy, associated with the cosmological constant  $\Lambda$ , compose the vast majority of the Universe today (68% and 27%, respectively) while normal matter composes only the remaining 5% (Peebles, 1993). Cold DM differs from Hot DM, another hypothetical type of DM, as the former is composed of particles moving much more slowly than the speed of light while the latter is composed of particles with ultrarelativistic velocities (Peebles, 1993). Several candidates have been proposed for DM since the idea of an invisible matter that interacts weakly with normal matter through gravity was introduced in modern physics, namely, weakly interactive massive particles (WIMPs), axions, sterile neutrinos and PBHs (de Swart et al., 2017). Notably, it was also proposed to modify the theory of gravity to account for the unexpected gravitational behaviours of astrophysical objects in the Universe (Milgrom, 1983). WIMPs were one of the first candidates to be suggested and as of today they still arouse great interest as demonstrated by the large number of current and future experiments performed in order to detect them. In fact, WIMPs are a well-supported candidate as they fit perfectly within the standard model and the history of the Universe (Craig & Katz, 2015). As of today, only indirect evidence of DM has been generated based on the observation of gravitational effects in the rotation curves of galaxies that could not be explained by current knowledge of gravity (Sofue, 2020). Nevertheless, there has been a claim of possible direct detection of DM from the DAMA/LIBRA experiment (Bernabei et al., 2010) that however still faces skepticism from the majority of the DM research community. Despite new staggering sensitivities have been reached by the XENONnT Dark Matter Search Experiment (Aprile et al., 2020), current and future experiments will be limited by the neutrino floor, the theoretical lower limit of WIMP-like DM models, which will make direct detection of WIMPs even more challenging (Billard et al., 2014). WIMPs can also be detected indirectly by searching for the products of WIMPs annihilation such as gamma rays, neutrinos and cosmic rays. The results of the PAMELA experiment in 2008 were attributed to a possible detection of DM as a rise of positrons was found in a cosmic ray whose energies matched the one of a possible DM annihilation (Cholis et al., 2009). However, the indirect detection of DM was never confirmed or rejected as of today. Overall, DM still eludes us today despite the great effort made in detecting it by the scientific community. New methods of probing DM are being proposed such as GW detection. In fact, as described more extensively below, DM can leave an imprint on the GW signals from compact binary inspirals and be captured from future-generation GW detectors (Kavanagh et al., 2020). The detection of such an effect on the GW signal could indirectly prove the existence of DM in the Universe.

## 1.2 Gravitational waves in vacuum

General relativity states that GWs are caused by the acceleration of masses and that the resulting distortion of space-time propagates through the Universe with the speed of light. Since GWs interact weakly with matter, they can travel for several millions of light years and reach GW detectors on Earth without disturbance (Gravitational Wave International Committee, 2019). Therefore, GWs offer a clear signal of cosmic events that are very distant from our galaxy. If the source of GW is assumed to be very distant from the observer, the local metric tensor  $g_{ij}$  will measure a nearly flat spacetime. As a result, a GW can be mathematically conceptualized as a small perturbation  $h_{ij}$  that is added onto a flat Minkowski metric tensor  $\eta_{ij}$  (Einstein, 1918):

$$g_{ij} = \eta_{ij} + h_{ij}. \quad (1)$$

The distortion has two linear polarizations denoted with the symbols  $+$ ,  $\times$  and vectors  $e_+$ ,  $e_\times$ , respectively. Thus, the perturbation  $h$  can be formulated as the superimposition of its two polarized components denoted with  $h_+$  and  $h_\times$ :

$$h_{ij}^{TT} = h_+ e_{ij}^+ + h_\times e_{ij}^\times. \quad (2)$$

The superscript  $TT$  means that the equation is defined in the transverse traceless gauge. The GW perturbation can also be defined by the quadrupole formula, which relates the amplitude of the perturbation to the mass distribution of the object generating it:

$$h_{ij}^{TT}(t, r) = \frac{2G}{(c^4 r)} \ddot{I}_{ij}^{TT}(t - r/c), \quad (3)$$

where  $r$  is the distance of the observer from the source,  $I(t - r/c)$  is the mass quadrupole moment defined on the retarded time  $t - r/c$ ,  $G$  is the gravitational constant and  $c$  is the speed of light (Carroll, 2004). Equation (3) implies that the mass generating a GW has to be distributed in an object such that the second time derivative of the mass quadrupole moment is non-zero. This occurs in cases of non-axisymmetric mass distribution such as in rotating neutron stars (Roy et al., 2020) and orbiting compact binaries, whereas objects with an axisymmetric mass distribution like isolated black holes have a zero quadrupole moment and therefore do not generate GWs.

### 1.2.1 Compact Binaries Inspiral Gravitational Waves

Compact binaries inspiral GWs (Fig. 1) are produced by pairs of orbiting objects that are both massive and dense such as stellar black holes, supermassive black holes, neutron stars and white dwarfs. Based on the current instrumentation, the most likely scenario to be detected is that the compact binary is made up of two neutron stars, two black holes, or a combination of them. Depending on the specific composition of the compact binary a completely different GW signal is generated. However, all compact binaries GWs share the same mode of generation: as the objects revolve around each other, a GW is produced and its amplitude and frequency increase as the objects orbit closer and faster until the merging event occurs. During this process, the gradual production of the GW radiation is responsible for the loss of orbital energy of the revolving objects<sup>1</sup>. The formulas associated with GW perturbation in  $+$  and  $\times$  directions are (Abernathy et al., 2011):

$$h_+(t) = \frac{2\nu M}{d_L} (1 + \cos^2 \iota) [M\omega(t; t_0, M, \nu)]^{2/3} \cos[2\phi(t; t_0, M, \nu) + \phi_0], \quad (4)$$

$$h_\times(t) = \frac{2\nu M}{d_L} 2 \cos \iota [M\omega(t; t_0, M, \nu)]^{2/3} \sin[2\phi(t; t_0, M, \nu) + \phi_0], \quad (5)$$

where  $M$  is the total mass of the binary system,  $d_L$  is the luminosity distance,  $\iota$  is the angle of inclination of the binary's orbital angular momentum with the line of sight,  $\omega$  is the angular velocity of the binary relative to its center of mass,  $\phi(t; t_0, M, \nu)$  is the orbital phase,  $t_0$  and  $\phi_0$  are constants relative to the time stage of merger and the orbital phase of the binary at that stage, respectively. Finally,  $\nu$  is the symmetric mass ratio.

---

<sup>1</sup>The first indirect observation of GWs was made by calculating over the years the loss of orbital energy of the Hulse-Taylor binary, which matched the predicted GW radiation from the binary (Weisberg et al., 2010).

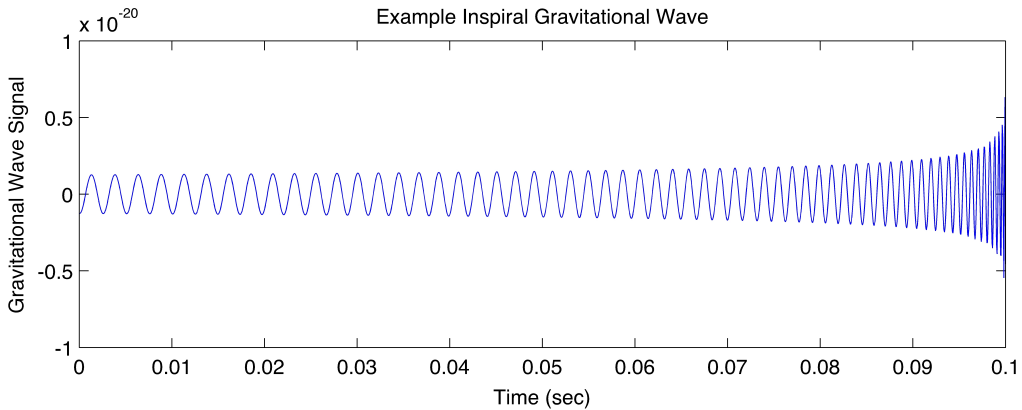


Figure 1: Example of a compact binary inspiral GW signal. Figure from LIGO Scientific Collaboration (2019).

The early phase of the inspiral is characterized by a nearly constant amplitude and angular frequency. This phase can last for weeks or years depending on the energy dissipation rate of the binary system.

### 1.3 Primordial Black Holes

PBHs are theoretical objects that are hypothesized to have formed in the early Universe, shortly after the Big Bang during the radiation-dominated era (Carr et al., 2021). Unlike stellar black holes, which are formed from the collapse of massive stars, PBHs are believed to have originated from the extreme density fluctuations in the early Universe. These black holes would form when regions of high density became gravitationally unstable after reaching a critical density value ( $\delta_c \approx w = 1/3$  in radiation-dominated era) and collapsed under their own gravity. The exact mechanisms leading to their formation are still a subject of research and debate among astrophysicists. PBHs could span an extremely wide mass range as denoted by the following generalized equation (Carr et al., 2021):

$$M \sim \frac{c^3 t}{G} \sim 10^{15} \left( \frac{t}{10^{-23} s} \right) g. \quad (6)$$

Equation (6) roughly corresponds to the Hubble mass in grams at time  $t$  and it shows that the mass of a PBH ( $M$ ) is dependent on the time of formation with respect to the beginning of the Universe. PBHs formed at Planck time ( $10^{-43} s$ ) would have the Planck mass ( $10^5 g$ ), while those formed at 1 s would be formed with a mass of  $10^5 M_\odot$ , comparable to supermassive black hole found at the center of galactic nuclei. PBHs are therefore intriguing objects that hold the potential to provide insights into fundamental physics and the early Universe. Despite being elusive and challenging to detect directly, scientists continue to explore various observational methods and theoretical models to better understand these hypothetical black holes. PBHs are also considered a potential candidate of DM due to their low mass range (Kavanagh et al., 2020). Several constraints due to physical effects such as Hawking radiation, cosmological effects like cosmic microwave background anisotropies, or certain astronomical observations (e.g. GW detections), have been measured on the mass of PBHs, thereby narrowing down the possible discoverable masses and mass fraction of PBHs in respect to the total DM in the Universe (Carr et al., 2021).

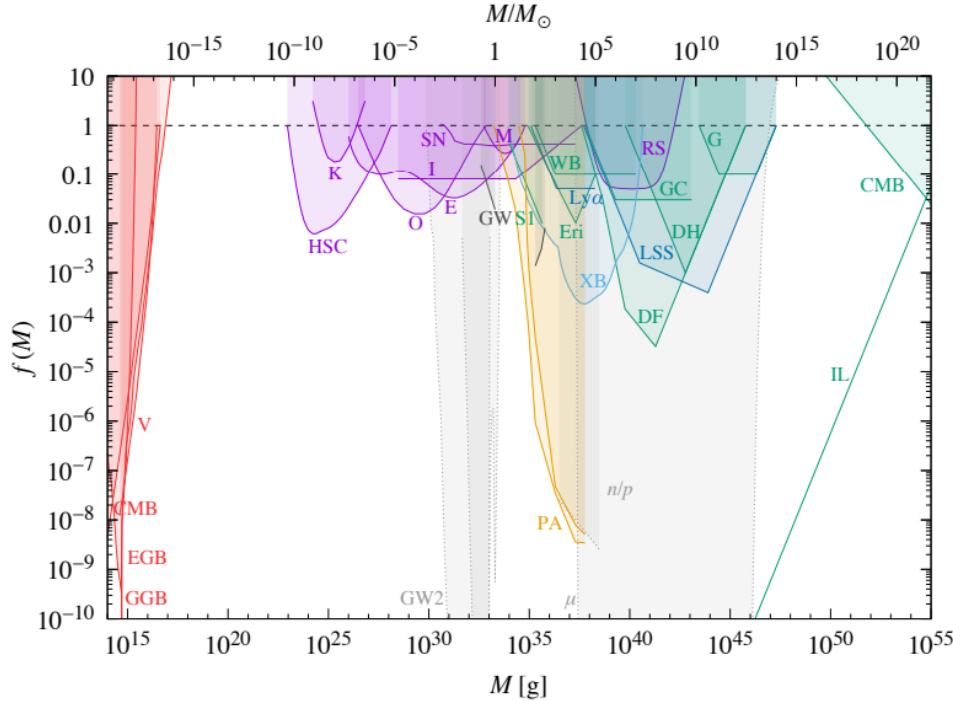


Figure 2: Constraints developed on PBH mass fraction from evaporation due to Hawking radiation (red), gravitational lensing (magenta), dynamical effects (green), GWs (black), PBH accretion (light blue), cosmic microwave background distortions (orange), large-scale structure (dark blue) and background effects (grey). Figure from Carr et al. (2021).

The plot depicted in Fig. 2 shows the results of all the calculated physical constraints on the mass fraction of PBH ( $f(M)$ ) in respect to the total DM in the Universe as a function of the PBH mass ( $M$ ). Throughout this master thesis project, the PBH mass fraction and PBH masses were assumed to fit into the constrained values shown in Fig. 2.

## 1.4 Gravitational waves with environmental effects

Several environmental effects of different nature can impact the GW signal of a BBH merger. The candidates of these external effects considered for this manuscript are DM spikes, gravitational atoms and accretion disks. It has been demonstrated that these effects influencing the dynamics of BBH inspirals are measurable and distinguishable in future GW detectors (Cole et al., 2022).

### 1.4.1 Dark matter spikes

DM spikes (Fig. 3), which are regions of overdensities of cold, collisionless matter, could form around various types of black holes, including supermassive, intermediate-mass, and stellar-mass astrophysical black holes, as well as hypothetical black holes of primordial origin. Previous studies have demonstrated the detectability of DM spikes through the drag force they apply on the BBH merger during the inspiral (Kavanagh et al., 2020). This effect, also known as gravitational dynamical friction, was first theorized by Chandrasekhar in 1943 to describe the motion of bodies in galactic dynamics (Chandrasekhar, 1943).

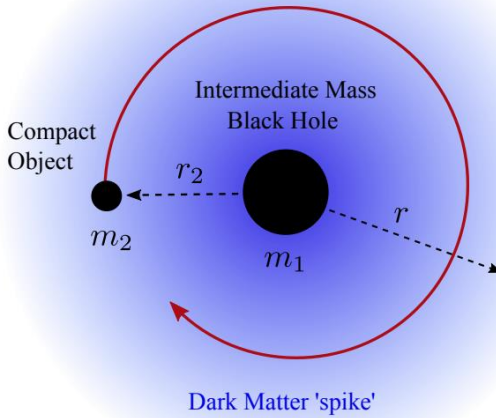


Figure 3: Example of an intermediate-mass ratio BBH merger with a DM spike. Figure from Kavanagh et al. (2020).

Essentially, when a massive body moves at a constant velocity through a medium composed of significantly less massive bodies, the smaller bodies exert a drag force on the moving mass. The resulting dynamical friction can be mathematically described by the following equation:

$$F_{DF} = -4\pi \ln \Lambda G^2 \frac{M_{body}^2 \rho}{v^2}, \quad (7)$$

where  $M_{body}$  is the mass of the moving body,  $\rho$  is the mass density of the medium,  $v$  is the velocity of the moving body and  $\ln \Lambda$  is the Coulomb logarithm, which contains information about the minimum and maximum impact parameters relevant for the dynamical friction force. This concept can be extended to the scenario of merging black holes inspiraling through a region of cold DM. The gravitational drag exerted from the DM particles in this case dissipates more energy as the black holes inspiral in towards each other, resulting in a faster inspiral compared to a vacuum case. Consequently, a noticeable dephasing of the GW signal detected is expected (Kavanagh et al., 2020). According to extensive studies on DM density profile and evolution, it can be hypothesized that the evolution of DM spike throughout the BBH merger should follow the model of a dynamic dress rather than a static model. As a result, a dynamic model is able to properly measure the energy transfer to the DM spike and the build-up of phase difference over time (Kavanagh et al., 2020). Therefore the assumption of a dynamic dark dress was used throughout this paper. The initial density profile of the DM spike around black holes as a function of the distance  $r$  from the central black hole is modeled with a power law:

$$\rho_{CDM}(r) = \rho_6 \left( \frac{r_6}{r} \right)^{\gamma_s}, \quad (8)$$

where  $\rho_6$  is the initial density profile of the spike at a reference distance of  $r_6 = 10^{-6}$  pc from the central black hole and  $\gamma_s$  is the slope of the spike (Cole et al., 2022). For the PBH case, the density profile follows the Equation (8) with a correction made to the  $\rho_6$ :

$$\rho_6 \propto \left( \frac{m_1}{M_\odot} \right)^{\frac{3}{4}}. \quad (9)$$

Therefore, in the PBH merger case, the DM spike density profile is proportional to the central black hole with mass  $m_1$ . The rate of energy loss of the BBH merger system with DM spikes is given by  $\dot{E}_{env} = \dot{E}_{DF}$ , where  $\dot{E}_{DF}$  is the energy lost due to dynamical friction and is described by the following equation:

$$\dot{E}_{DF} = \frac{4\pi G^2 m_2^2 \rho_{CDM}(r, t) \xi(v) \ln \Lambda}{v}, \quad (10)$$

where  $m_2$  is the mass of the second black hole,  $\rho_{CDM}(r, t)$  is the DM spike density as a function of distance  $r$  from the central black hole and time,  $v$  is the orbital velocity of the moving black hole and  $\xi(v)$  is the fraction of DM particles moving more slowly than  $v$  (Cole et al., 2022).

#### 1.4.2 Gravitational atom

Ultralight bosons represent one of several proposed candidates for DM as they can form long-lived condensates known as 'clouds' around rotating black holes (Baumann et al., 2022). The existence of ultralight particles with masses as low as 10-20 eV could potentially explain the weak gravitational interaction observed with ordinary matter. Black holes present a unique opportunity to investigate these ultralight DM particles through a phenomenon called superradiance (Fig. 4). When a black hole is spinning, it can lose its angular momentum if a boson with a specific mass exists within the range of physical states that would match with the rotational frequency of the black hole (Baumann et al., 2022). As a result, the bosonic cloud can absorb rotational energy from the black hole through the Penrose process (Vicente et al., 2018) and undergo a stimulated emission, generating more bosons in an amplified manner. Superradiance, in this context, acts as an intriguing method to investigate DM states that would otherwise be challenging to explore experimentally.

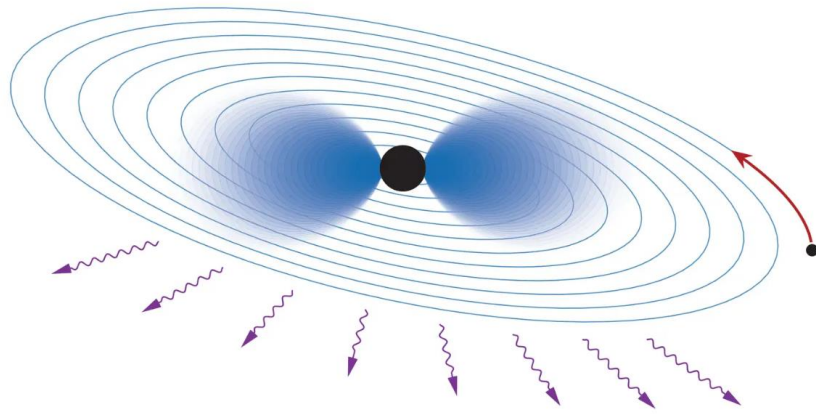


Figure 4: Artistic representation of gravitational atom ionization with a central black hole surrounded by a bosonic cloud. Figure from Baumann et al. (2022).

The recent findings from the Event Horizon Telescope (Event Horizon Telescope Collaboration et al., 2019) collaboration concerning the spin of the supermassive black hole in the galaxy M87 offer the opportunity to explore and constrain this interesting regime of ultralight DM masses. Besides GW emissions, two effects are considered in the black hole binary evolution surrounded by a bosonic cloud: the ionization of the cloud caused by the gravitational perturbation of the secondary moving body, and the accretion of the cloud caused by the smaller black hole as it moves through it. The rate of energy lost over time can be expressed as  $\dot{E}_{env} = \dot{E}_{ion} + \dot{E}_{acc}$ , where  $\dot{E}_{ion}$  and  $\dot{E}_{acc}$  correspond to the rate of energy loss due to the ionization and the accretion, respectively (Cole et al., 2022).

#### 1.4.3 Accretion disks

Accretion disks of baryonic matter are widely known to form around supermassive black holes. Unlike DM, the dephasing effect for accretion disks is caused by gas torques instead of dynamical friction. Still, the resulting effect on GW signal needs to be distinguished from dephasing caused by DM spikes as the two environmental effects exhibit similarities during the merging phase of the inspiral (Cole et al., 2022). In the context of accretion disks around black holes, Lindblad resonances and Type I migration are phenomena that can significantly influence the behavior of matter orbiting black holes. Lindblad resonances occur in accretion disks when there is a match between the orbital frequency of the matter in the disk and the natural frequency of an oscillatory mode in the disk. When these frequencies align, they create regions of enhanced density or particle concentration within the disk (Hirata, 2011). These resonances can induce the accumulation or scattering of material in specific locations, influencing the disk's structure and leading to the formation of density waves or spiral arms. Lindblad resonances in the accretion disk can affect the distribution and movement of matter around merging black holes. This redistribution of material can potentially alter the dynamics and orbital evolution of black holes as they approach each other, impacting the eventual merging process.

Type I migration refers to the inward migration or movement of smaller astronomical objects (like planets or planetesimals) embedded within an accretion disk due to their interactions with the disk's material. In the context of black holes, it can also involve smaller black holes or stellar-mass compact objects orbiting within the accretion disk (Yamada & Inaba, 2010). Type I migration influences the orbital evolution of these smaller objects, causing them to either move inward toward the central black hole or migrate outward. This migration process is dependent on the interactions between the embedded objects and the surrounding disk material. In the scenario of a black hole merger, both Lindblad resonances and Type I migration within the accretion disks could impact the merging of the black holes (Cole et al., 2022). The energy loss of the BBH merger system over time due to the effect of the accretion disk is given by:

$$\dot{E}_{torque} = \frac{G^{1/2}T_0m_1^2}{4r^{3/2}(m_1 + m_2)^{1/2}}, \quad (11)$$

where  $T_0$  is the total net torque on the secondary black hole,  $m_1$  and  $m_2$  are the masses of the components of the BBH and  $r$  is the distance from the central black hole. Specifically,  $T_0$  can be expressed as follows:

$$T_0 = -\Sigma(r)r^4\Omega^2q^2M^2, \quad (12)$$

where  $M$  is the Mach number of the disk,  $\Sigma(r)$  is the surface density of the disk,  $\Omega$  is the orbital angular velocity of the disk and  $q$  is the mass ratio of the merger (Cole et al., 2022).

## 1.5 First and second generation detectors

The first generation of GW detectors are Virgo (Caron et al., 1997), the Laser Interferometer Gravitational-Wave Observatory (LIGO) (Abbott et al., 2009) and GEO600 (Willke et al., 2002). They use an L-shape Michelson interferometer configuration to detect the distortion of space caused by passing GWs on Earth. Over the years, LIGO and Virgo have been upgraded to a sensitivity 10 times higher than before, making it possible to detect for the first time a GW generated by a black hole merger GW150914 in 2015 (Abbott et al., 2016). This event finally proved Albert Einstein's theories from 1916 and opened the door to the new field of GW observation. Thanks to these key improvements, the number of detected signals and the volume of detectable space has increased, which has led to the beginning of the era of second generation (2G) detectors. Seven more BBHs detections occurred after the first GW detection. These were followed by the GW170817 in 2017, which was the first ever detected GW formed by a binary neutron stars (BNS) merger (Abbott et al., 2017b). This successful detection answered some important questions about the astrophysics of neutron stars. The GW detection was followed immediately by a direct observation of electromagnetic waves (Abbott et al., 2017a), thereby inaugurating a new era of multimessenger astronomy and proving the correlation between BNS merging and gamma-ray emissions. Although GEO600 did not directly participate in these discoveries (i.e. it never succeeded at detecting GWs due its design limits), GEO600 is still responsible for ongoing research for laser interferometry technologies that are also used in 2G detectors (Affeldt et al., 2014). The Kamioka Gravitational Wave Detector (KAGRA) later joined the LIGO-Virgo collaboration in 2020. It was the first detector to implement cryogenic technology and to be built underground, which reduces thermal and seismic noise. KAGRA has a range of detectable BNS up to 25 Mpc and BBH up to 260 Mpc. With future upgrades, it is estimated that KAGRA will reach sensitivity for BNS at 130 Mpc and for BBH at 1200 Mpc (Abbott et al., 2018).

Overall, LIGO and Virgo are sensitive in the GW frequency bandwidth of  $\sim$ 20-2000 Hz. However, they exhibit significant limitations: below 10 and above 200 Hz their sensitivity curves are dominated by noise coming from seismic events or shot noise, respectively. In addition, their lower cutoff frequency of 20 Hz restricts the detectable total mass of binaries to be less than  $200 M_{\odot}$  (Abernathy et al., 2011). As described in the section above, the dephasing effect due to environmental effects is mostly visible at lower frequencies during the early phase of the inspiral. Therefore, current GW detectors are not suitable for detecting environmental effects, which further justifies the use of next generation detectors to probe DM in GW emissions for the purpose of the master thesis research described in this manuscript.

## 1.6 Future Gravitational Wave detectors

With the increasing number of advanced detectors, the sky localization of GW sources will become even more accurate and efficient (Abernathy et al., 2011). At the moment, LIGO and Virgo are sensitive to BNS at a maximum distance of 100 Mpc and 30 Mpc, respectively, and to BBH at a maximum distance of 910 Mpc and 270 Mpc, respectively. With the future upgrades LIGO and Virgo could reach detectable distances for BNS up to 330 Mpc and 260 Mpc respectively and for BBH up to 2500 Mpc and 2100 Mpc (Abbott et al., 2018).

The Einstein Telescope (ET) (Fig. 5), in the next decade, will open a new generation of detectors known as third generation (3G). ET will then be joined by Cosmic Explorer and the Laser Interferometer Space Antenna (LISA) in the future. With its revolutionary triangular configuration, it will have a sensitivity factor  $\sim 20$  better than Virgo and a lower cutoff frequency of 1-3 Hz. The wider frequency band of ET will enable detecting the full inspiral, merger and post-merger of GW signals emitted from BNS, allowing to study tidal properties and the nature of the dense matter found in neutron stars. ET will be sensitive to BNS up to a large distance (more

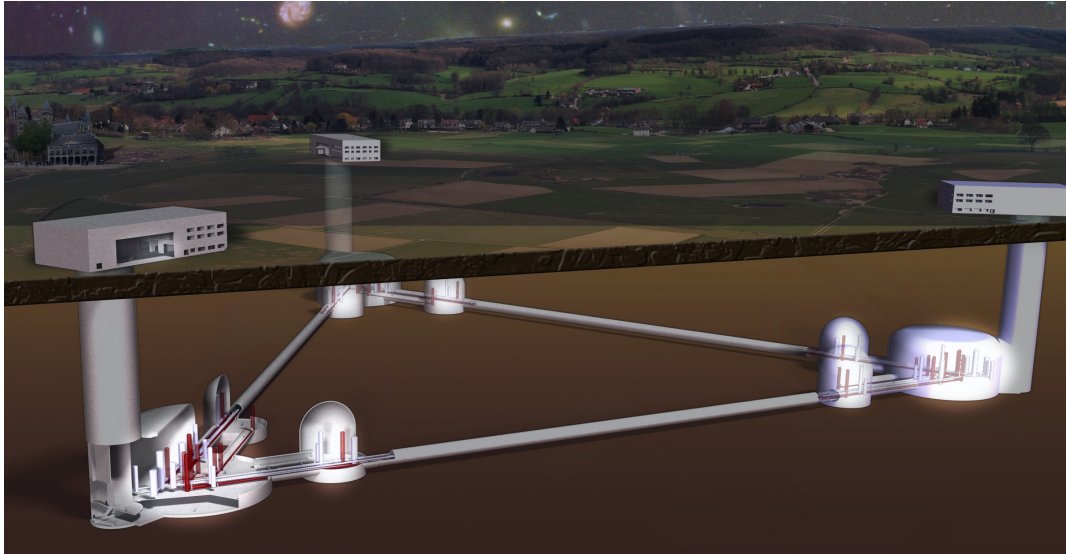


Figure 5: Artistic layout of ET. Figure from Abernathy et al. (2011).

than 8000 Mpc, redshift<sup>2</sup>  $z \sim 2$ ). Therefore, there will be more detections of GWs generated by BNS and, as a result, information about the nucleosynthesis process and physical origin of jet (emission of particles) in merging BNS could be inferred. With the aid of other astronomical observatories, 3G detectors will enable to study the demographics and formation mechanism of BNS (Gravitational Wave International Committee, 2019). The detectable distance of BBH will increase up to 84 Gpc ( $z \sim 0.3\text{--}20$ ), namely from the peak of the star formation rate up to the dark cosmological era, and up to one million black hole mergers per year could be observable. Therefore, a larger catalogue of GWs coming from BBH will be available giving information about the their formation and their evolution throughout different cosmic times. Moreover, as the observable range of masses will be greater, stellar-mass black holes could potentially be connected with the supermassive black holes found in the centers of galaxies by detecting intermediate-mass black holes with mass interval  $10^2\text{--}10^4 M_{\odot}$ . Thanks to its improved sensitivity in the low-frequency range, it could detect stochastic GWs with a higher accuracy as it could reach levels of strength of the GW stochastic background  $\Omega_{GW}^3 \sim 10^{-12}$  at around frequencies of 10 Hz. ET will be sensitive to burst GWs coming from supernovas at 5 Mpc and therefore it is estimated that one per year of this kind of waves will be detectable. Finally, ET is predicted to be sensitive to continuous GWs generated by pulsars mostly at 10 Hz (Abernathy et al., 2011). ET will therefore be able to detect all kinds of GWs with the exception of signals generated by binary supermassive black holes. The latter are believed to possess a merging frequency of

<sup>2</sup>Let us consider an astrophysical source, at a distance  $d$  from the Earth, that emits electromagnetic radiation at a given wavelength  $\lambda_e$ . As a consequence of the expansion of the Universe, this radiation gets stretched along its travel towards the Earth, where it is measured equal to  $\lambda_o$ . The ratio between the observed wavelength  $\lambda_o$  and the emitted wavelength  $\lambda_e$  is given by:  $(1 + z) = \lambda_o/\lambda_e$ , where  $z$  is defined as the redshift of the source. At small distances from the Earth, the redshift and the distance of a source are related by the following relation:  $z = dH_0/c$

<sup>3</sup>Stochastic GW background is produced by superposition of independent signals due to unresolved astrophysical sources of GWs at different redshifts. This kind of waves can give information about the evolution of compact objects through cosmic times and they are thought to have an irregular shape that resembles a noise signal. The strength of the stochastic background is characterized by the dimensionless quantity  $\Omega_{GW}$ , which is the ratio between the energy density  $\rho_{gw}$  in GWs and the critical energy density of the Universe  $\rho_c = 3H_0^2/8\pi G$ .

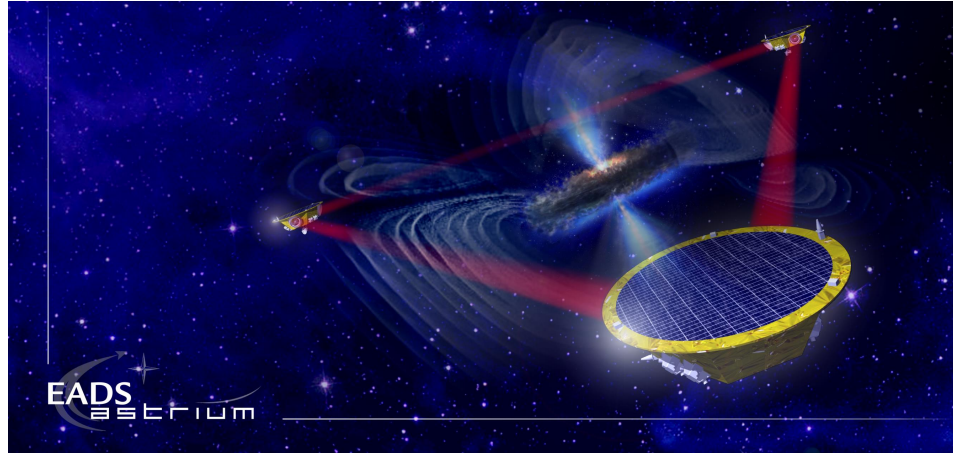


Figure 6: Artistic layout of LISA. Figure from European Space Agency (2019).

the order of mHz, which is out of range of ET but will be detectable by LISA (Gravitational Wave International Committee, 2019). LISA, the first space-based gravitational-wave observatory, will consist of three satellites forming a triangular detector with arms extending 2.5 million kilometers and therefore will represent the largest interferometer to be ever constructed (Fig. 6). The detector's layout has been designed to enable the observation of various GW sources within the frequency band of 0.1 mHz to 0.1 Hz. This frequency range is associated with diverse GW sources in the Universe, including supermassive black hole binaries, extreme mass ratio inspirals (EMRIs) consisting of smaller black holes orbiting and merging with significantly larger black holes, ultra-compact binaries within the Milky Way, black hole binaries in their pre-merger stage, the stochastic GW background and possibly exotic compact objects (Barack et al., 2019). By capturing GWs emanating from the farthest reaches of the Universe, LISA will profoundly advance our comprehension of the Universe's origins, evolution and structure (Amaro-Seoane et al., 2017).

In summary, with the arrival of 3G detectors, the possibilities of making new discoveries in astrophysics and fundamental physics are enormous. For instance, as it would be able to detect more GW signals, ET could use them as standard sirens, namely tools to better measure the expansion of the Universe and the Hubble constant. Moreover, ET could help solving contradictions between general relativity and quantum physics by gathering new data from black holes. Finally, it could test general relativity, find a better mass bound on the hypothetical graviton, place a more accurate constrain on the time variability of the gravitational constant and investigate the nature of DM by potentially discovering DM spikes (Gravitational Wave International Committee, 2019). For the purpose of this thesis, we will focus on the simulation of ET sensitivities data as the GW signal generated from the mass ratio of PBH merger chosen for this thesis fit well with the ET sensitivity bandwidth.

## 1.7 Matched Filtering formalism

The mechanism of signal disentanglement mostly used by 2G detectors is the matched filtering technique (Babak et al., 2006). The main assumption of the matched filtering formalism is that the strain  $s(t)$  measured by a GW observatory can be mathematically modelled as the result of

the strain of a GW signal  $h(t)$  added onto the noise  $n(t)$  of the detector:

$$s(t) = n(t) + h(t). \quad (13)$$

The physical meaning of the strain corresponds to the length distortion that the arms of an interferometer undergo as a GW travels through Earth resulting in a measurement of a signal. It is measured by dividing the extension of the interferometer's arm ( $\Delta l$ ) by its normal length ( $l$ ):  $s = \Delta l/l$ . The strain is what a GW detector plots over time in its output. Matched filtering works by taking the desired GW signal out of the background noise picked up from the detector on Earth. The process relies on scanning through a wide template bank of thousands of gravitational waveforms. For any chosen waveform template  $T(t)$  it is possible to compute its signal-to-noise ratio (SNR) namely the ratio of the template's amplitude over the strength of the noise:

$$SNR = \int_{-\infty}^{\infty} \frac{\tilde{s}(f)\tilde{T}(f)e^{i2\pi f t_0}}{S_n(f)} df, \quad (14)$$

where  $s(f)$  is the strain of the detector,  $S_n(f)$  is the power spectral density (PSD) of the noise,  $f$  is the frequency domain over which the integration is done and  $t_0$  is the time in which the strain is recorded. The tilde notation indicates that the formula deals with the Fourier transform to the frequency domain of each term. The PSD refers to the power distribution over the detectable frequency spectrum of a detector. It is also common to compute the amplitude spectral density (ASD) which is the square root of the PSD output values. The ASD of the noise can be interpreted as the sensitivity of the detector to GW signals. In fact, the noise amplitude when processed into its ASD is converted into its frequency domain. The corresponding graph then shows the strength of the frequencies associated with the noise oscillations plotting a curve. All detectable GW signals will lie over this sensitivity curve (Fig. 7). Equation (11) shows that by multiplying the output of a GW detector by a waveform and then integrating the results, the SNR will be higher if this waveform is present. The presence of the expected GW signal would then be confirmed.

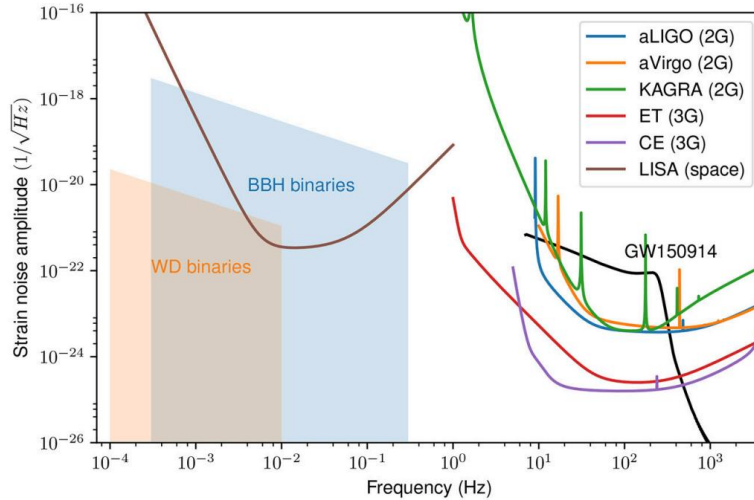


Figure 7: Estimated ASD for ET (red), Cosmic Explorer (purple), LISA (brown), Advanced LIGO Hanford/Livingston (blue), Advanced Virgo (orange) and Kagra (green). The blue and orange regions correspond to detection sensitivity zones for massive BBH and white dwarf binaries, respectively. The black line is associated with the strain amplitude of GW150914 (Abbott et al. (2016)). Figure from Ezquiaga & Zumalacarregui (2018).

## 1.8 Bayesian Inference

In conjunction with matched filtering, Bayesian inference is used to estimate BBH physical parameters from raw GW signals. Bayesian inference is a statistical approach in which Bayes' theorem is used to update the probability for a hypothesis as more information becomes available. Bayes' theorem is a fundamental principle in probability theory that describes the relationship between conditional probabilities of events or hypotheses (Robert et al., 2010). It is expressed as follows:

$$P(A|B) = \frac{P(B|A) \cdot P(A)}{P(B)}, \quad (15)$$

where  $A$  and  $B$  are hypotheses or events,  $P(A|B)$  is the probability of  $A$  given that  $B$  is true,  $P(B|A)$  represents the probability of  $B$  given that  $A$  is true,  $P(A)$  and  $P(B)$  are the probabilities of  $A$  and  $B$ , respectively. Bayesian inference can therefore be applied to test hypotheses based on observed data and its key components are:

- **Prior distribution  $P(A)$ :** it contains our initial knowledge or assumptions about a hypothesis before observing any data.
- **Likelihood function  $P(B|A)$ :** describes the probability of observing the data given different values of the parameters associated with the data.
- **Posterior distribution  $P(A|B)$ :** the updated distribution that combines the prior distribution and the likelihood function. It represents our beliefs about the hypothesis after incorporating the observed data.

One of the strengths of Bayesian methods is their ability to incorporate prior knowledge into the statistical analysis, allowing them to handle uncertainty and make more informed decisions (Robert et al., 2010). Bayesian inference finds applications in various fields, including machine learning, data analysis and scientific research and it has been widely used for several tasks such as parameter estimation, hypothesis testing, regression analysis and probabilistic modeling. More importantly, it has been used in previous work related to GW parameter estimation and DM detection (Cole et al., 2023). Recently, the adoption of Bayesian approaches has increased due to advancements in computational techniques and Markov chain Monte Carlo (MCMC) methods, which have facilitated the implementation and analysis of complex Bayesian models in astronomy (Sharma, 2017). Overall, Bayesian inference offers a powerful and flexible framework to draw conclusions from data in a systematic and coherent way. However, Bayesian methods can be computationally intensive, especially for complex models with high-dimensional data.

## 1.9 Machine Learning

Machine learning (ML) is a subset of artificial intelligence and is the field of study that "*gives computers the ability to learn without being explicitly programmed*" (Patterson & Gibson, 2017). ML algorithms can be divided into two main categories: supervised and unsupervised. Supervised ML performs classification or regression tasks by learning from samples of labeled data. On the other hand, unsupervised ML can learn relationships automatically from non-labeled data. ML is routinely used in computer science for performing tasks such as big data analysis and image processing, as well as in other domains including Biology, Economics, Robotics, etc. (Jin et al., 2018). Deep learning (DL) is a branch of ML that is concerned with a class of algorithms that are inspired by the functioning and structure of the human brain known as artificial neural networks (ANN) (Patterson & Gibson, 2017). Convolutional neural networks (CNNs) are a specialized type of ANN that can be successfully employed in a wide range of ML tasks, including classification

of text and both 2D and 3D images. It has been demonstrated that CNNs can successfully be used for the detection and parameters estimation of GWs, achieving similar sensitivities and lower errors compared to matched-filtering, while being more computationally efficient (George & Huerta, 2018). CNNs have also been used to identify transient signal glitches, which are a special type of noise that resembles the shape of GW signals (Razzano & Cuoco, 2018). One limitation of CNNs is that they require labeled training data. As an alternative, it is worth looking into autoencoders as they are a type of ANN that can be directly trained on unlabeled data in an unsupervised fashion. In particular, Shen et al. (2017) successfully applied an autoencoder for denoising GW signals associated with BBH mergers. Overall, DL models can efficiently process and learn from large datasets, which are typically found in GW research. Additionally, ML methods often outperform traditional Bayesian methods due to their ability to identify complex patterns in the data. These two aspects justify the use of ML methods within the context of this master thesis research.

### 1.9.1 Neural Networks

Neural networks are composed of several layers of connected artificial neurons (Fig. 8) that work by taking several inputs  $x_1, x_2, x_3 \dots x_n$  and producing a single output.

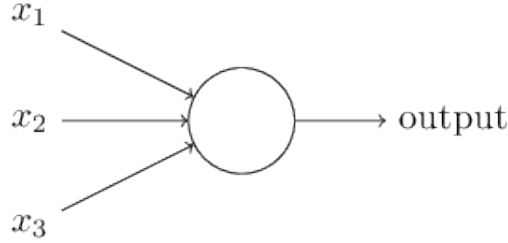


Figure 8: Diagram of a single neuron. Figure taken from Nielsen (2015).

In order to determine how the output is related to the inputs, a weight  $w_j$  is attributed to each input  $x_j$ . The neuron's output will be 0 or 1 if the weighted sum of the inputs is lower or greater than a specific threshold value.

$$\text{output} = \begin{cases} 0 & \text{if } \sum_j w_j x_j \leq \text{threshold} \\ 1 & \text{if } \sum_j w_j x_j > \text{threshold} \end{cases} \quad (16)$$

Equation (12) can be simplified by introducing the bias ( $b$ ) which is equal to the negative value of the threshold and also by writing the weighted sum notation with a dot product,  $w \cdot x \equiv \sum_j w_j x_j$ . The output of a neuron after these modifications is then equal to:

$$\text{output} = \begin{cases} 0 & \text{if } w \cdot x + b \leq 0 \\ 1 & \text{if } w \cdot x + b > 0 \end{cases} \quad (17)$$

Optionally a neuron applies a mathematical function called activation function  $\sigma$  to its output such that the output is:  $\sigma(w \cdot x + b)$ . As mentioned earlier, multiple neurons are then connected in layers forming a multi-layer neural network (Fig. 9). The input layers will give an output which will be the input for inner layers. The inner layers will send an output to the next layer until the output layer is reached. In this way a neuron in the second layer can make a more complex decision than a neuron in the first layer and even more abstract decisions can be made by the neurons in the third layer. In this way, network of neurons with several layers can perform elaborated

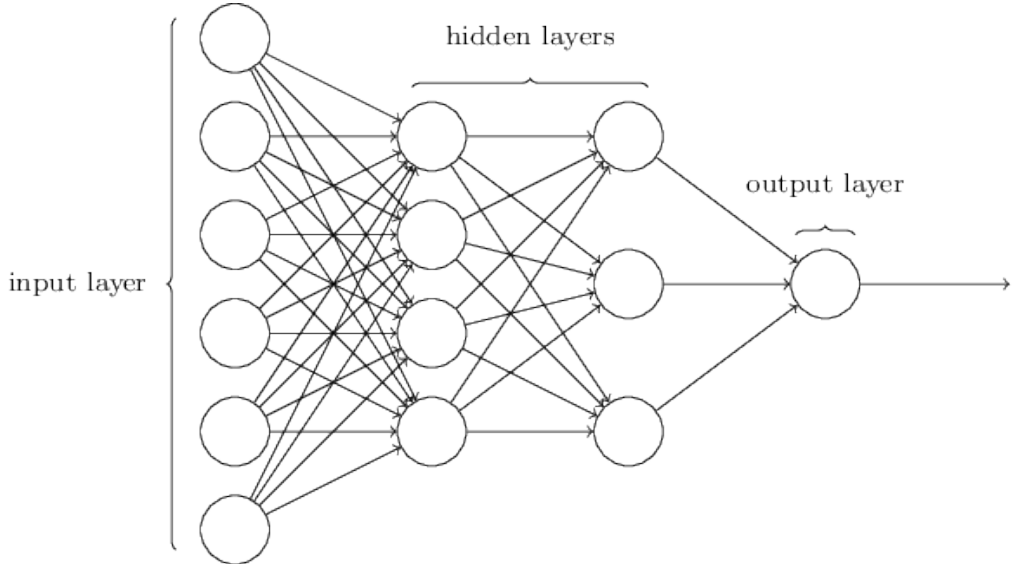


Figure 9: Diagram of a multi-layer neural network. Figure from Nielsen (2015).

decision making. This neural network information transfer is called feedforward and it is also the most common and most powerful way of data elaboration by a multi-layer neural network (Nielsen, 2015). After choosing the architecture of the network, the DL algorithm requires a training dataset in order to learn to recognize certain types of features. All data can be pre-labeled in different categories so that the the network learns to attribute each type of data to certain labels. This is the essence of supervised ML as the network is guided to classify only certain classes of data. A second set of data called validation set can be used to provide an unbiased evaluation of the trained model while regulating the weights of the neural networks. Finally, a third set of unseen data called the testing set is used to give an unbiased evaluation of the final trained model.

In order to determine the best sets of weights and biases of the neurons so that the output of the network approximates defined target values  $y$ , we can define the loss function as:

$$L(w, b) \equiv \frac{1}{2n} \sum_x \|y(x) - a\|^2, \quad (18)$$

where  $w$  corresponds to the set of weights of the network,  $b$  are the biases,  $n$  is the total number of training inputs and  $a$  is the output of the network when  $x$  is the input. In the case of targets being labels 0 or 1, the neural network can be modelled such that its output lies in an interval of values with endpoints corresponding to the two label values. By looking at Equation (14), the loss function appears to become smaller when the output is closer to the target value. The aim is therefore to find weights and biases that minimize the loss function as much as possible in order to train the network effectively. The gradient descent algorithm allows to perform such task (Goodfellow et al., 2016). Suppose a loss function  $L$  is defined on a collection of generic variables  $v_1, v_2, v_3 \dots v_n$  represented by  $v$ , the algorithm will try to find a new set of variables  $v'$  which makes  $L$  smaller. In order to do so it first defines the deviation  $\Delta L$  from the initial value of  $L$  with the following approximation:

$$\Delta L \approx \nabla L \cdot \Delta v, \quad (19)$$

where  $\nabla L$  is the gradient operator applied on  $L$  and defined on all the old variables  $v_1, v_2, v_3 \dots v_n$  and  $\Delta v$  represents the deviation from the initial values of variables  $v$ .  $\Delta v$  is defined as:

$$\Delta v = -\eta \nabla L, \quad (20)$$

where  $\eta$  is the learning rate, a small and positive parameter. By applying Equation (19) in Equation (18),  $\Delta L$  is always kept negative and  $L$  decreases at every iteration of the algorithm. Finally, the new set of variables  $v'$  will be defined as:

$$v' = v - \eta \nabla L. \quad (21)$$

The algorithm will keep updating the variables associated with the loss function using Equation (20) until a local or global minimum of  $L$  is reached. Equation (20) shows that the functioning of the gradient descent algorithm is highly dependent on the value of the learning rate which is arbitrary. Such value needs to be small enough so that the approximation in Equation (19) is held but also not too small so that the algorithm does not update  $v$  too slowly (Nielsen, 2015).

### 1.9.2 CNN architecture

CNNs are usually made up of several layers of neurons that carry out specialized functions (Fig. 12). The convolution layer is usually the first layer that input data encounters in a CNN. In this layer the convolution operator represented by a matrix named filter or kernel is applied on the input data (Patterson & Gibson, 2017). The filter is then slid over the whole input and, unless padding is applied, this produces a smaller output compared to the initial input (Fig. 10). During training the values of the convolution filters are updated (equivalently to updating weights in neurons) to minimize the CNN loss function. After every convolution step,

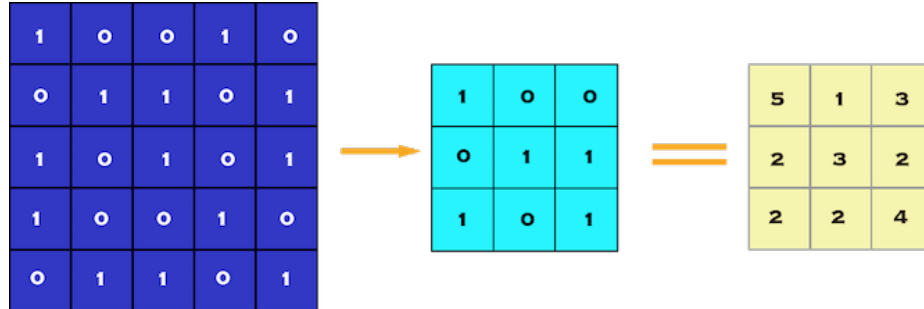


Figure 10: Diagram of a 3x3 convolution filter applied on a 5x5 input. The convolution operation consists in multiplying the overlapping entries of the filter and of the input within the filter window and then adding the results. An output containing all the convolution results is generated from sliding the filter over the whole input. Figure from Yalçın (2018).

an activation function called Rectified Linear Unit (ReLU) is usually added. This activation function is applied on each entry of the convolution output and consists in replacing all negative values with zero. The purpose of adding a ReLU is to introduce non-linearity since the output of the convolution step is linear but the aim of the CNN is to describe real world data that is non-linear. It is also common to add a pooling layer (Fig. 11) after the convolution to reduce dimensionality of the input and computational power associated with the processing of the data, keeping the most important information of the input at the same time (Patterson & Gibson,

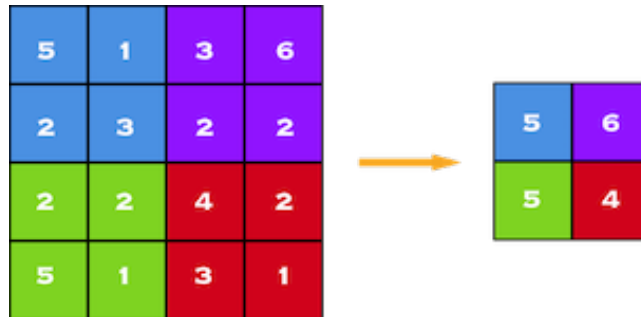


Figure 11: Diagram of a Max Pooling step with 2x2 filter size. The filter is applied on each entry of the input. Then it will take the highest value of the input within the filter window and create an output containing all the values taken from sliding the window over the whole input. Figure from Yalçın (2018).

2017). Pooling can be of different types: max, average, sum, etc. However, max pooling is found to be the most effective in many CNN applications.

The layers of convolution followed by ReLU and pooling can be repeated several times inside the same CNN in order to refine the input even more and improve the overall performance. With every convolution step it is also common to define the number of filters desired to be applied on the data. In this way several activation maps are produced containing different enhanced features. The activation maps are then stacked together forming an output volume with a certain 'depth' equal to the number of convolution filters defined. As described above, pooling changes the dimensionality of the output volume. However, it does not change the depth of the output volume. When the stacked activation maps undergo another convolution step, the filter is applied along the depth dimension producing a single new activation map for every filter defined in the new convolution step. Typically the last layer of a CNN is a fully connected (FC) layer, which allows to classify the features extrapolated from the input by the convolution steps. Each FC layer is also associated with an activation function such as ReLU and softmax.

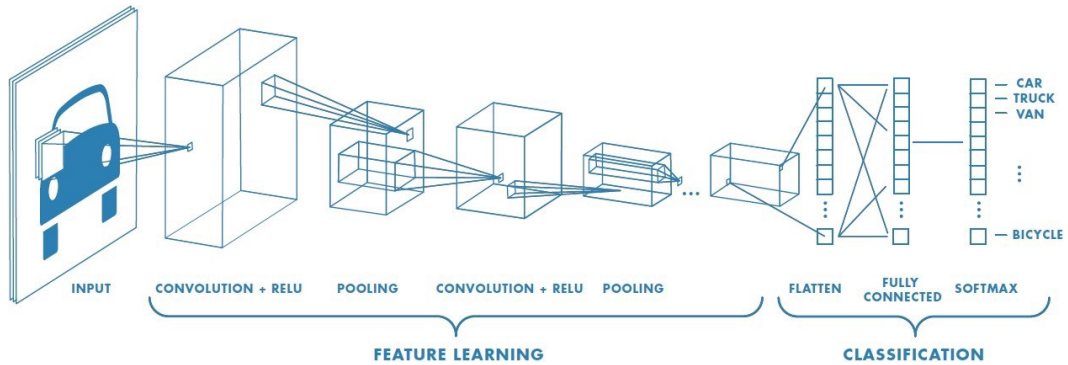


Figure 12: Example of a CNN applied on an image. Figure from Saha (2018).

The softmax activation function  $a_j^N$  of the j-th output neuron at layer  $N$  is defined as:

$$a_j^N = \frac{e^{z_j^N}}{\sum_k e^{z_k^N}}, \quad (22)$$

where  $z_j^N$  is the weighted sum of the inputs and  $z_k^N$  represents the output of the neurons. The weighted sum of the inputs is defined as  $z_j^N = \sum_k w_{jk}^N a_k^{N-1} + b_j^N$ , where  $N$  and  $N - 1$  stand for two consecutive connected layers,  $w_{jk}^N$  is the weight from the k-th neuron in  $N - 1$  layer to the j-th neuron in the  $N$  layer,  $a_k^{N-1}$  is the activation function of the k-th neuron in the  $N - 1$  layer and  $b_j^N$  is the bias of the j-th neuron in the  $N$  layer (Nielsen, 2015). The softmax mathematical expression works such that the sum of the activation functions values belonging to the same output layer is guaranteed to be always equal to 1. This can be expressed in the following algebraic form:

$$\sum_j a_j^N = \frac{\sum_j e^{z_j^N}}{\sum_k e^{z_k^N}} = 1. \quad (23)$$

If the activation function value of one neuron of the output layer increases, the activation function values of the other neurons of the same layer will decrease by the same amount in order to ensure that the overall sum of the activation functions of the neurons of that output layer is 1. The softmax function can therefore be interpreted as a way to normalize some input values into a vector of values that follows a probability distribution (Nielsen, 2015). Therefore, the application of a softmax activation function is suitable for the use of CNNs for classification problems.

## 1.10 Regression Analysis

Linear regression is a statistical method used to find a linear relationship between independent and dependent variables (Kuchibhotla et al., 2019). CNNs can be adapted for regression problems by using a mean squared error (MSE) loss function defined by:

$$MSE = \frac{1}{n} \sum_{i=1}^n (y_i - \hat{y}_i)^2 \quad (24)$$

where  $n$  is the number of samples in the dataset,  $y_i$  represents the actual target value of the  $i$ th sample and  $\hat{y}_i$  is the predicted value for the  $i$ th sample. The CNN architecture can be modified in order to predict a target value with an unrestrained output range by setting an identity activation function to the output neuron. The identity activation function is defined as  $f(x) = x$ , where the output is equal to the input value without applying any non-linear transformation. The overall accuracy of a CNN model on unseen data for the estimation of target values can be calculated by using different statistical tools such as the coefficient of determination ( $R^2$ ), the mean-absolute-error (MAE) and the root mean square error (RMSE). The corresponding equation of  $R^2$  is given by:

$$R^2 = 1 - \frac{SS_{res}}{SS_{tot}} \quad (25)$$

where  $SS_{res} = \sum_{i=1}^n (y_i - \hat{y}_i)^2$  and  $SS_{tot} = \sum_{i=1}^n (y_i - \bar{y})^2$ , in which  $\bar{y}$  is the mean of the target values. When  $R^2=1$ , it indicates that the model perfectly predicts the dependent variable based on the independent variable(s). On the other hand, when  $R^2=0$ , it suggests that the model does not explain any variability in the dependent variable (Kuchibhotla et al., 2019). A high  $R^2$  would

be represented by most of the predicted points lying on the identity line of a scatter plot of the dependent against independent variables. The equation for the MAE and RMSE are given by:

$$MAE = \frac{1}{n} \sum_{i=1}^n |y_i - \hat{y}_i| \quad (26)$$

$$RMSE = \sqrt{\frac{1}{n} \sum_{i=1}^n (y_i - \hat{y}_i)^2} \quad (27)$$

therefore, a MAE and RMSE tending to zero show that model well predicts the testing target values (Kuchibhotla et al., 2019).

### 1.11 Project aims

As the number and duration of GW signals are expected to increase substantially in 3G detectors such as LISA, Einstein Telescope and Cosmic Explorer, the matched filtering method currently used in conjunction with Bayesian inference for detecting GWs signals and performing BBH physical parameter estimation will no longer be sufficient as it would require a huge amount of computational time. In fact, as mentioned above, the matched filtering formalism requires scanning over a large template bank of several candidate gravitational waveforms that would best fit with the output of a GW detector. Therefore, a new technique for performing faster GW signal detection and BBH parameter estimation is urgently needed (Chayan Chatterjee & Datta, 2019). As mentioned in Section 1.1, GW signal detection could be an important tool in probing DM. However, no dephasing effect in compact binary inspiral GW signals has been detected yet due to the limits of 2G detectors, while it is predicted that LISA and ET will be capable of observing the inspiralling phase of black hole mergers for more extended periods, thereby enabling comprehensive studies of the dephasing effect due to DM spikes. Furthermore, PBHs are intriguing astrophysical objects that offer room for potential new discoveries about the early Universe. In addition, ML could be suitable for efficiently recognizing the features of dephased GW signals. In summary, this research aimed to demonstrate, in alternative to classical methods of matched filtering, that the application of a CNN model is an efficient method to estimate the DM spike physical parameters of dressed PBH mergers as they would be detected by ET.

## 2 Methods

The first dataset used for training the proposed DL algorithm in this work consisted of 25,000 GW signals of simulated PBH binary mergers generated on the frequency domain with arbitrary value ranges for DM spike parameters ( $\rho_6$  and  $\gamma_s$ ), as outlined in Table 1. The PBH binary physical parameters were set to constant  $\mathcal{M}$  and  $q$  values, where  $q$  is the mass ratio of the PBH binary merger defined as  $q = m_2/m_1$  and  $\mathcal{M}$  is the chirp mass defined as  $\mathcal{M} = \frac{(m_1 \cdot m_2)^{3/5}}{(m_1 + m_2)^{1/5}}$  in which  $m_1$  and  $m_2$  are the masses corresponding the central more massive PBH and the orbiting less massive PBH, respectively. The  $\rho_6$  and  $\gamma_s$  values were spread on 25 bins in a log scale and linear scale space, respectively, to generate signals evenly in the arbitrary value ranges.

Parameter	Value range
$\gamma_s$	[2.1, 2.5]
$\rho_6 [M_\odot / pc^3]$	$[10^{11}, 10^{15}]$
q	$10^{-3}$
$\mathcal{M} [M_\odot]$	0.0028

Table 1: GW parameters ranges for Dataset 1.

A second dataset consisted of 31,250 GW signals generated by performing a full parameter search by also varying the  $q$  parameter of the PBH binary within the chosen value range as shown in Table 2.

Parameter	Value range
$\gamma_s$	[2.1, 2.5]
$\rho_6 [M_\odot / pc^3]$	$[10^{11}, 10^{15}]$
$log_{10}q$	[-4.5, -2.5]
$\mathcal{M} [M_\odot]$	[0.0020, 0.032]

Table 2: GW parameters ranges for Dataset 2.

The amplitude of the GW signals as a function of frequency was defined by the following equation:

$$h_0(f) = \frac{1}{2} \frac{4\pi^{2/3} G^{5/3} \mathcal{M}^{5/3} f^{2/3}}{c^4} \sqrt{\frac{2\pi}{\ddot{\Phi}}}, \quad (28)$$

where  $\Phi$  is the phase of the GW signal. The length of the PBH binary inspiral was set to 7 days for both datasets. The choice of setting the duration of the inspiral to 7 days was motivated by previous research where it was concluded that 7 days worth of GW signal allows to generate enough detectable build-up of dephasing due to the presence of DM spike in PBH binary inspirals (Cole et al., 2023). Similarly, the luminosity distance of all simulated GW events was fixed to  $d_L=229$  Mpc (Cole et al., 2023). The gravitational waveforms were then normalized by a factor of  $\sqrt{4/5}/d_L$  to account for the luminosity distance and to average the amplitude of the signal by the inclination angle between the detector on Earth and the GW event in the sky. The PBH merger signals were generated with the `pydd` Python library, which allows to create different environmental effects and to simulate a dynamic dark dress (A. & B., 2021). The result of the raw GW data simulation pipeline is shown in Fig. 13.

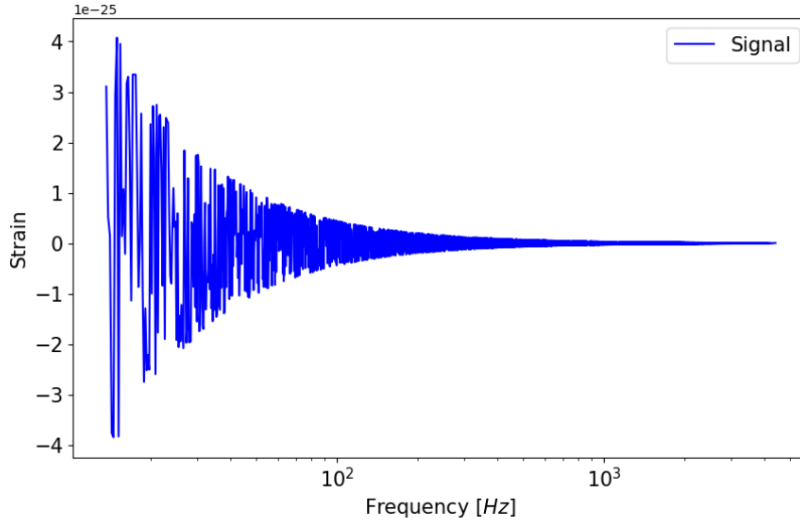


Figure 13: Simulated GW signal. The y-axis represents the  $h_+$  GW polarization amplitude and the x-axis represents the GW frequency. The plotted GW signal is defined from the frequency associated with the beginning of the PBH merger until the  $f_{ISCO}$  (in this case 13.7 Hz and 4397 Hz, respectively). As shown in the figure, the signal shape is not well refined due to the limited number of frequency bins over which the GW is defined.

The ET noise was generated in the frequency domain by simulating a Gaussian distribution using the ASD data from expected ET-D configuration (Hild et al., 2011) and by adapting code retrieved from the PyCBC library (Usman et al., 2016) such that it would be compatible with numpy Python code. The generated GWs were then embedded in several ET noise instances in order to perform data augmentation (Iglesias et al., 2023). In particular, in the first dataset, each GW associated with a certain combination of  $\rho_6$  and  $\gamma_s$  was repeated 40 times by adding new randomly generated ET noise, while in the second dataset the augmentation of each GW signal was carried out 2 times. The amplitude spectral density of the simulated ET noise is shown in Fig. 14. The plot is in agreement with the predicted ET sensitivity range between 1 and 5000Hz, as depicted in Fig. 7, and displays peak detection performance between 10 and 200Hz where most of the GW signal features are contained as shown in Fig. 13. The simulated output noise over frequency (Fig. 15) is consistent with the ASD plot where an increase in noise amplitude is visible at high frequencies of the ET sensitivity bandwidth, indicating that the sensitivity of the detector degrades as frequency increases.

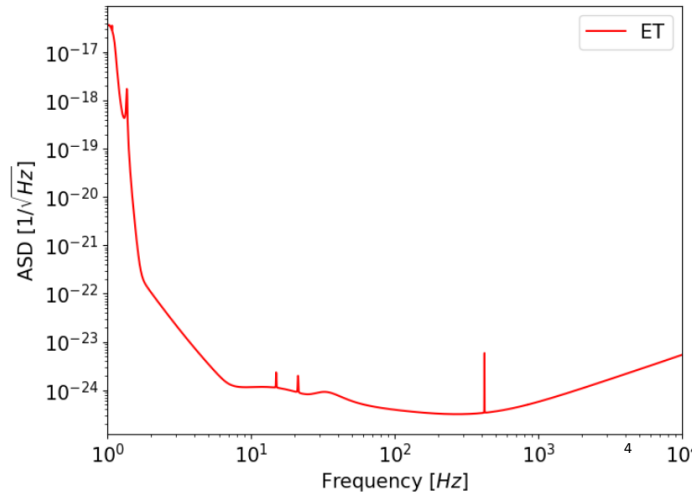


Figure 14: Amplitude spectral density of simulated ET noise. The y-axis is the characteristic strain of the detector and the x-axis is the detectable GW frequency. The spectral peaks are due to suspension thermal noise. The loss of sensitivity at low frequency is mostly attributed to a combination of quantum and seismic noise while at high frequency is solely due to quantum noise (Hild et al., 2011).

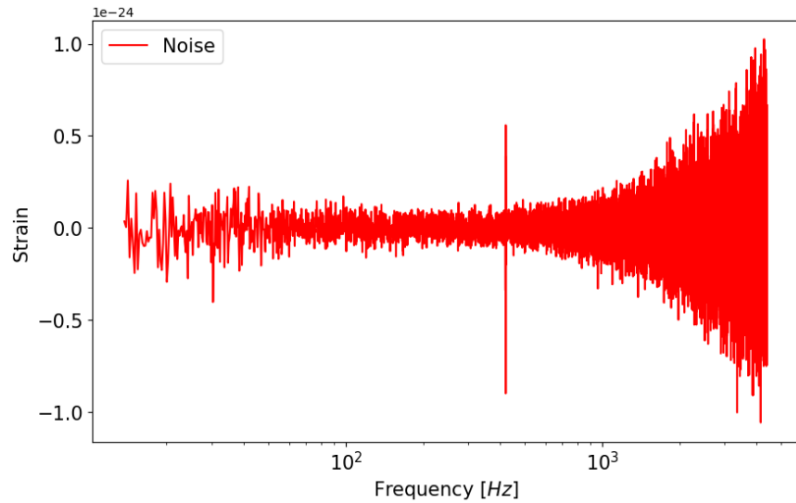


Figure 15: Simulated ET frequency series noise. The graph exhibits the sensitivity curve of the simulated ET detector as shown by the noise peaks at  $\sim 20$  Hz and  $\sim 400$  Hz as well as the increase of noise amplitude above 1000 Hz.

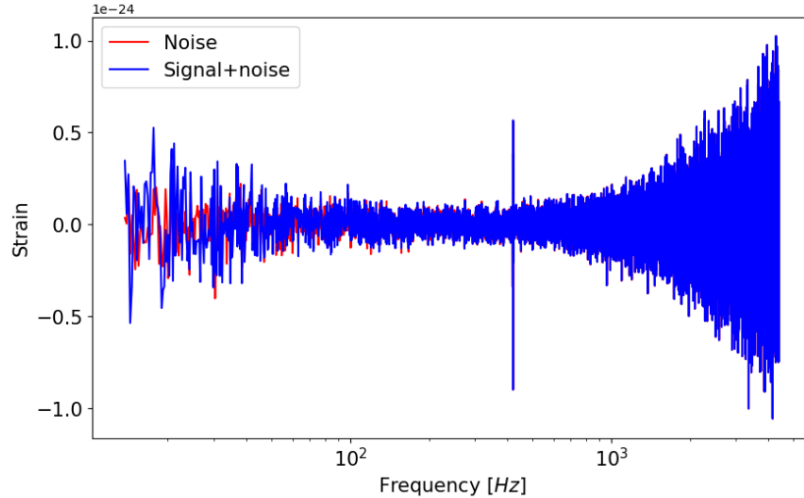


Figure 16: Simulated ET noise with injected GW signal (Blue) plotted over ET noise (Red). The shape of the GW signal is clearly distinguishable below 100 Hz.

By overlapping the signal and noise frequency series (Fig. 16), it is possible to see how the GW signal impacts the overall simulated detector output. Fig. 16 shows that the GW signal is mostly covered by noise from 100 Hz above. Therefore, each signal amplitude was computed over 20000 frequency bins linearly spread from the lowest frequency at which the merger starts until 100 Hz rather than until the  $f_{ISCO}$ <sup>4</sup> of the PBH merger as initially planned.

In order to perform a data quality check, the dephasing due to DM spikes was measured by calculating the phase difference between the signal with DM spike injection and a signal in vacuum with the same PBH binary parameters. This was carried out with the aid of the pydd Python library, which enables to instantly calculate the phase of a GW generated with an environmental effect or in vacuum. Then, a combination of random (Bergstra & Bengio, 2012) and grid search with 3-fold cross-validation (Pedregosa et al., 2011) over the space of hyperparameter values was performed in order to find the optimal CNN architecture for GW parameters estimation. Grid search is the process of scanning all possible permutations of hyperparameter values (in our case, number of convolution layers, number of dense layers, number of neurons in dense layers, filter size and number, batch size, learning rate as shown in Table. 3) and selecting the one that gives the highest score on the selected evaluation metric. k-fold cross validation allows to divide the training set and iterate with a model of the grid search k times. At each iteration a different subset of the input data is selected as training while the rest is used for validation (Kohavi, 1995). This process allows to provide a more robust estimate of the performance of each DL model generated from the grid search. The result of the grid search is shown in Table. 4 and Fig. 17.

The proposed CNN architecture for DM spike detection used in this master research project, which will be named as DM-CNN throughout this manuscript (Fig. 17), starts with a convolution layer including 32 filters of size 5x1, with a ReLU activation function followed by a max pooling layer with filter size 2.

---

<sup>4</sup>The frequency at the Innermost Stable Circular Orbit ( $f_{ISCO}$ ) is associated with the orbital frequency of the last stable circular orbit before the two PBHs coalesce or merge into a single object.

Hyperparameter	Value range
Learning rate	$[10^{-3}, 10^{-4}]$
Batch size	[16, 32]
#Convolution layers	[1, 2, 3]
Convolution kernel size	[2, 5, 10]
Convolution filters	[16, 32]
# FC layers	[1, 2, 3, 4]
FC neurons	[64, 128, 256, 512]

Table 3: Hyperparameter value list tested in the grid search.

Hyperparameter	Value
Learning rate	$10^{-4}$
Batch size	32
#Convolution layers	1
# FC layers	4
# Epochs	20
Optimizer	Adam
Loss function	MSE

Table 4: Main hyperparameters and associated values used for training the optimal CNN

A flatten layer is then added in order to reshape the output volume to a one-dimensional array. This is followed by four FC layers with 256, 128, 64 and 1 neurons, respectively. The first three FC layers have a ReLU activation function, while the last FC layer uses an identity activation function in order to give a single value estimate of the GW parameters. The CNN network was implemented with the `Keras` neural network library (Chollet et al., 2015) written in Python. The training of the DM-CNN was performed with the values of the hyperparameters listed in Table 4 using 70% of each dataset was used for training while the remaining 30% was split in 15% for validation and 15% for testing. Taking into account previous literature, a learning rate of  $10^{-4}$  is suitable considering that the recommended range of values is between 1 and  $10^{-6}$  allowing the gradient descent algorithm to work properly (Bengio, 2012). The Adam (Adaptive Moment Estimation) optimizer was chosen because it is a very efficient and commonly used optimization algorithm (Kingma & Ba, 2014). The MSE is a type of loss function specifically targeted for regression as explained above (Hodson, 2022). The batch size corresponds to the number of processed input samples based on which the network weights are updated during training. It should be set to multiples for either 2, 4, 8, 16 or 32 (Patterson & Gibson, 2017). A value of 32 for the batch size was therefore a suitable choice based also on prior results obtained with the computing infrastructure used by the hosting university research group. The number of epochs corresponds to how many times the network is applied on the same training and validation set in their entirety in order to find the most optimal set of weights that minimize the loss function. After some experimentation, it was found that increasing the number of epochs above approximately 20 did not improve validation loss, therefore a value of 20 epochs was used in all the experiments. The loss values calculated on the training and validation sets were plotted in order to monitor the fitting process. In general, a good fit to the data is achieved when training and validation losses decrease to values close to zero. Overfitting corresponds to the scenario in which training loss keeps decreasing while validation loss stops improving and reaches a plateau, meaning that the network is only fitting well on the training set and does not generalize well on

unseen data. On the other hand, underfitting occurs when training is not successful as indicated by high values of training and validation loss. During the research project, the training process was generally set up such that it would stop if the validation loss stopped decreasing to prevent overfitting. Both the grid search and training of the DM-CNN were conducted with the aid of the Snellijs GPU partition (SURF, 2024). After the fitting process was completed, the DM-CNN was applied on the testing set in order to provide an estimate on the studied DM spike and PBH binary parameters for each input data sample. In order to evaluate the performance on test data, the predicted output was compared against the associated true parameter value. The evaluation metrics used to understand the performance of the model in the estimation of the  $\rho_6$ ,  $\gamma_s$  and  $q$  parameters are the coefficient of determination score, mean-absolute-error and root-mean-squared error. Finally, a specific metric, called *Accuracy* throughout this manuscript, was designed in order to measure an accuracy-like value for each test bin ( $y$ ) using the following equation:  $Accuracy = RMSE/y$ . This was done in order to compare our results against the ones generated with matched filtering in conjunction with Bayesian inference (Cole et al., 2023).

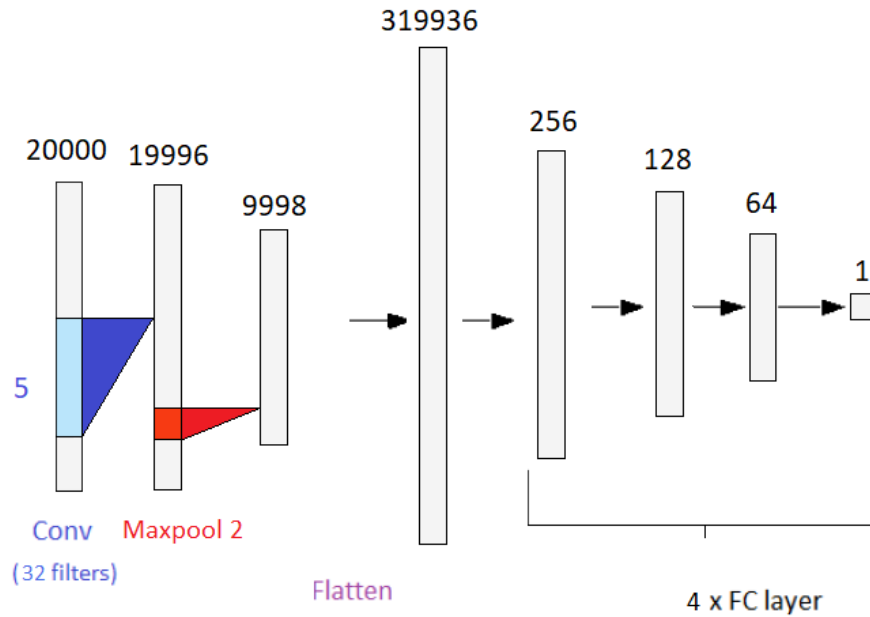


Figure 17: Diagram of the DM-CNN architecture following grid search of hyperparameters values used for this research. Numbers on top represent the first dimension of the output shape assuming that the second dimension is 1. Numbers on side, if present, represent the filters size.

### 3 Results

Firstly, as a sanity check the dephasing of the simulated GW signals with DM spike (Fig. 18) was plotted against the frequency bins of the GW signal. As it can be seen, there is a significant phase difference with respect to vacuum confirming that DM spike correctly influences the phase of the GW signal throughout the entire frequency band. In fact, it is theorized that a wave cycle difference between a GW signal in vacuum and a GW signal with DM spike corresponding to  $\Delta\phi=2\pi$  is sufficient to estimate the DM dress parameters (Kavanagh et al., 2020). Therefore, it can be concluded that the data was simulated correctly and is in accordance with previous related work that used the same data (Cole et al., 2023).

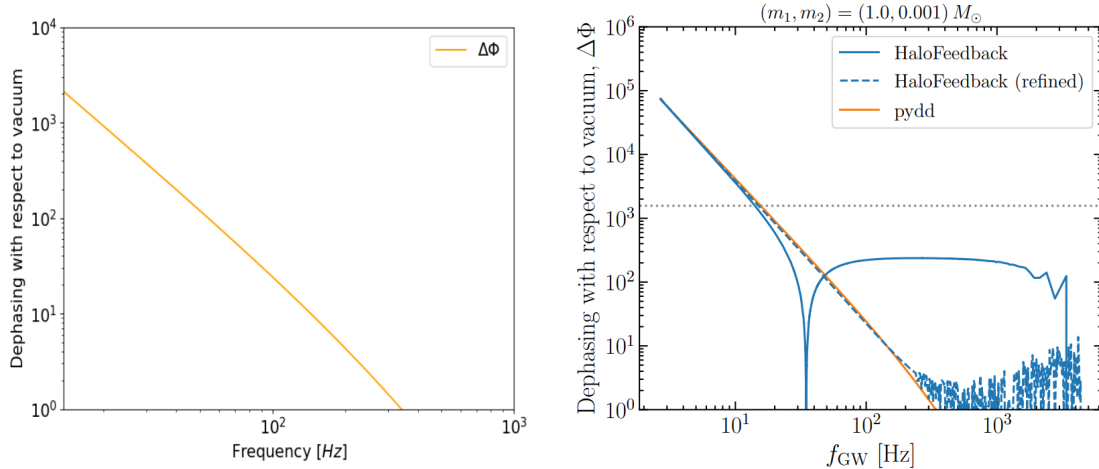


Figure 18: Dephasing plot of the simulated GW signal with DM spike in this master thesis project (left) and from Cole et al. (2023) (right). The orange lines in both panels are generated with `pydd` using the same BBH and DM spike parameters ( $m_1=1M_\odot$ ,  $m_2=10^{-3}M_\odot$ ,  $\rho_6=1.396\times10^{13}M_\odot/pc^3$  and  $\gamma_s=2.25$ ) while the blue lines on the right panel are generated with the `HaloFeedback` model (Kavanagh, 2020).

#### 3.1 Dataset 1

This section presents the application of the methods outlined in Section 2 using dataset 1. The main objective is to get an insight on the performance of the DM-CNN in estimating the parameters of the GW signals with DM dress. The DM-CNN training dynamics depicted in Fig. 19 show the change of the loss and validation loss functions as the epochs increase.

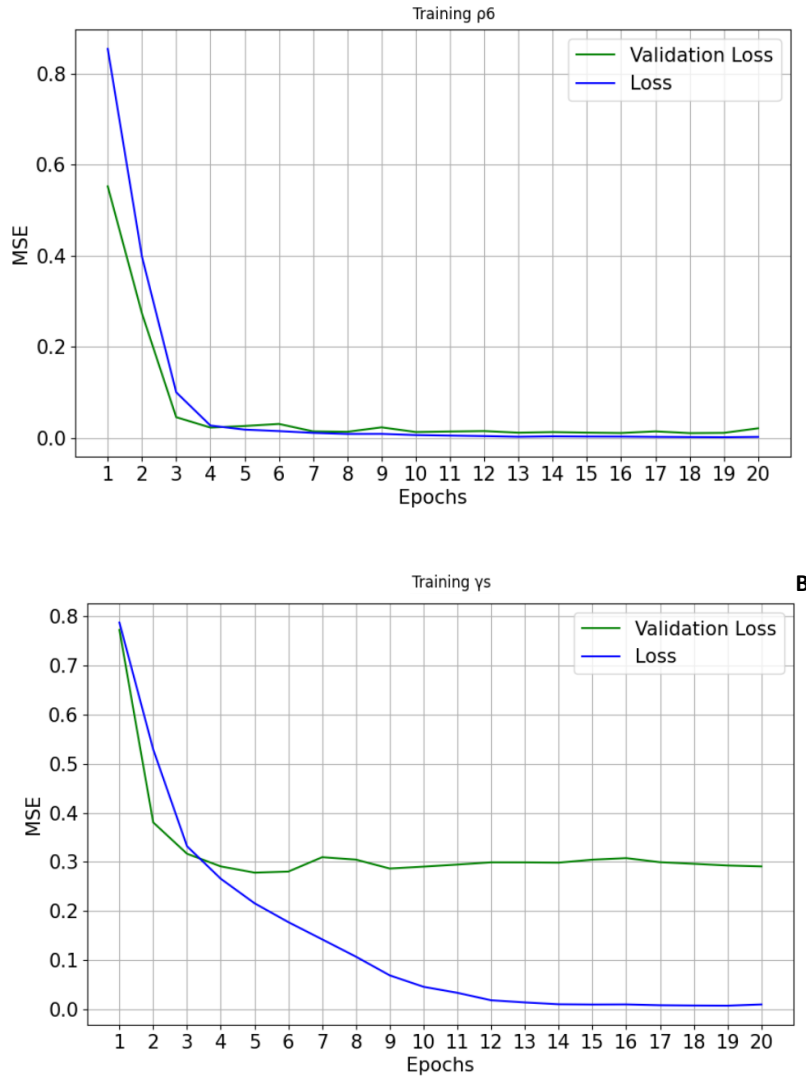


Figure 19: Training dynamics plots using  $\rho_6$  (A) and  $\gamma_s$  (B) as target variable. The best model weights were retrieved at the epoch corresponding to the lowest validation loss value.

The plots of DM-CNN training dynamics on dataset 1 show that the model has a better fit to the data with  $\rho_6$  used as target variable compared to the  $\gamma_s$ . In fact, during the training of the DM-CNN when  $\rho_6$  is used as target variable, the training and validation losses both followed a decreasing trend tending to 0. On the other hand, the training dynamics of the DM-CNN when  $\gamma_s$  parameter is used as target variable shows that validation loss reached a plateau at around 0.3, meaning that the prediction on the validation data was less accurate and the algorithm was not able to generalize as effectively on unseen data. Overall, the training dynamics plot indicates that the proposed DL algorithm successfully extracted and learned information from the training set and is able to predict the target values of the validation set to a good extent for both parameters. The parameter estimation results given from the application of the DM-CNN on the testing set

of dataset 1 can be found in Fig. 20.

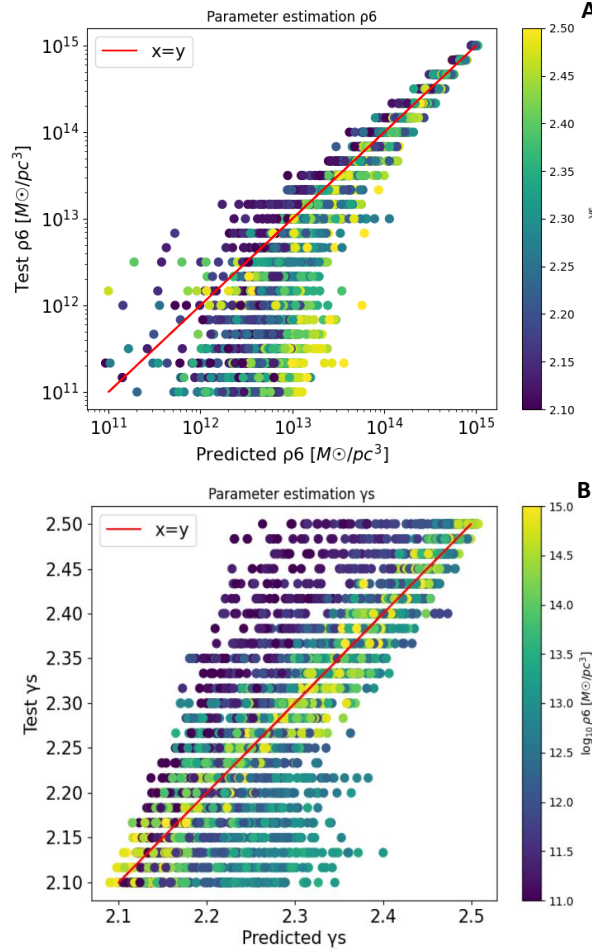


Figure 20:  $\rho_6$  (A) and  $\gamma_s$  (B) parameter estimation results. The y-axis represents the test values associated with the target variables. The x-axis contains the information about the predictions from the DM-CNN about each test target value. The color of the scatter plots represents the corresponding  $\gamma_s$  (A) and  $\rho_6$  (B) values of the test data, respectively. Plot A shows a clear tendency of the DM-CNN towards overestimating  $\rho_6$  target values.

Fig. 20 A shows a good prediction of  $\rho_6$  test values in the range  $10^{14}$ - $10^{15} M_\odot/pc^3$  independently of the associated  $\gamma_s$  values. On the other hand, the prediction of the  $\gamma_s$  (Fig. 20 B) test values is significantly worse, with the exception of  $\gamma_s$  test values associated with  $\rho_6$  values in the range  $10^{14}$ - $10^{15} M_\odot/pc^3$ . The *Accuracy* of the DM-CNN for each bin of the parameters value range calculated on the testing set is displayed in Fig. 21.

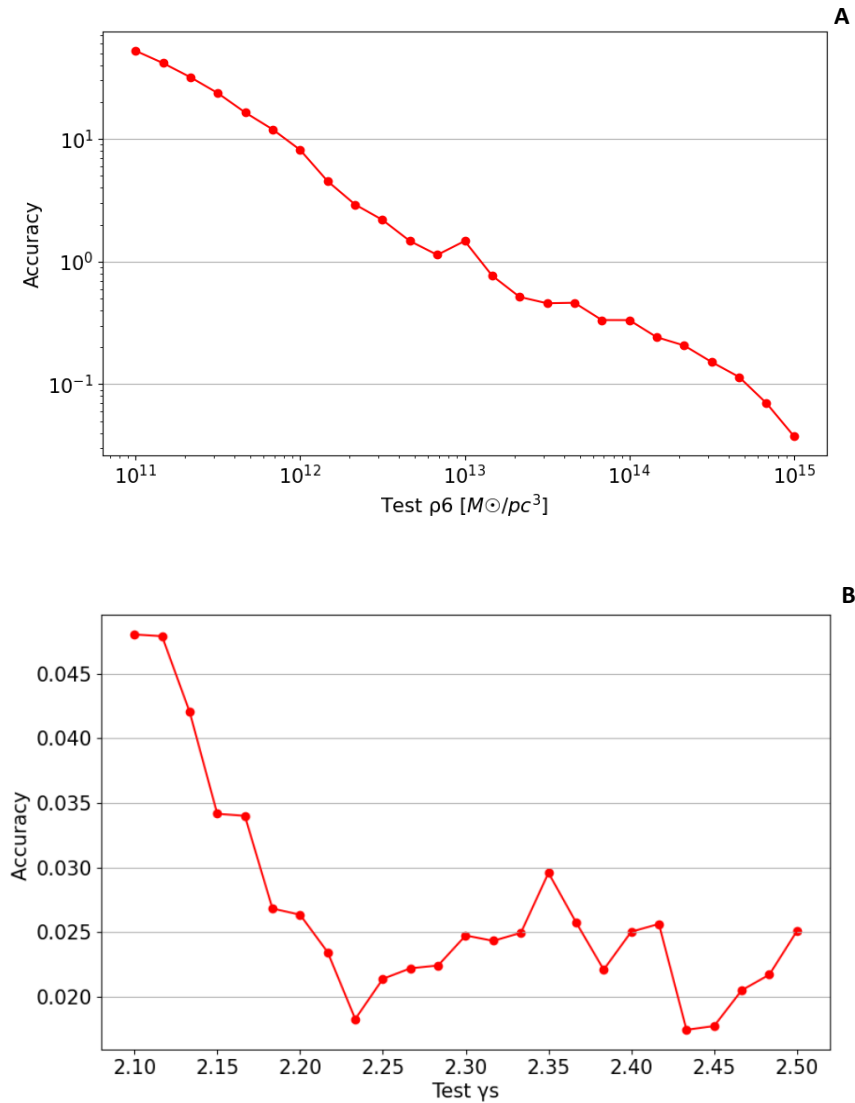


Figure 21: Accuracy plots associated with  $\rho_6$  (A) and  $\gamma_s$  (B) parameter estimation. The x-axis contains the test bin value and the y-axis contains *Accuracy* values associated with each test bin. The steepness can be interpreted as an increase or decrease in accuracy in predicting test values.

The *Accuracy* plot for  $\rho_6$  (Fig. 21 A) is consistent with the DM spike parameters estimation plots shown above, as the *Accuracy* of the DM-CNN improves with increasing  $\rho_6$  values. The *Accuracy* plot for  $\gamma_s$  (Fig. 21 B) shows two regions of best estimation of  $\gamma_s$  test values, specifically between 2.20 and 2.25 and between 2.425 and 2.45. Moreover, the  $R^2$  score is higher for the estimation of  $\rho_6$  compared to the estimation of  $\gamma_s$  as shown in Table 5. The training dynamics and parameter estimation plots obtained from the training of the DM-CNN with the constant PBH binary mass fraction  $q$  used as target variable can be found in Fig. 25 and Fig. 26 in the Appendix.

Metrics	$\rho_6$	$\gamma_s$	$q$
$RMSE$	$2.43\text{e}13 \text{ [M}_\odot/\text{pc}^3]$	0.06	$1.38\text{e-}06$
$MAE$	$1.36\text{e}13 \text{ [M}_\odot/\text{pc}^3]$	0.04	$1.09\text{e-}06$
$R^2$	99.0%	72.0%	/

Table 5: Evaluation metrics computed for Dataset 1. The  $R^2$  score associated with the  $q$  testing is left blank since  $R^2$  tends to infinity when all target variables share the same value.

### 3.2 Dataset 2

This section presents the application of the methods outlined in Section 2 using dataset 2. The training dynamics plots (Fig. 22) show that the DM-CNN did not train successfully when using the  $\rho_6$  and  $\gamma_s$  parameters as target variables. This can be deduced by the fact that the validation loss stops decreasing after a few epochs and then even starts increasing, which essentially means that the DM-CNN overfitted on the training set and therefore performed poorly on the validation set. On the other hand, Fig. 22 C shows that the DM-CNN generalized well on unseen data when using  $q$  as target variable as denoted by the drop of the validation loss to 0 after the first 2 epochs.

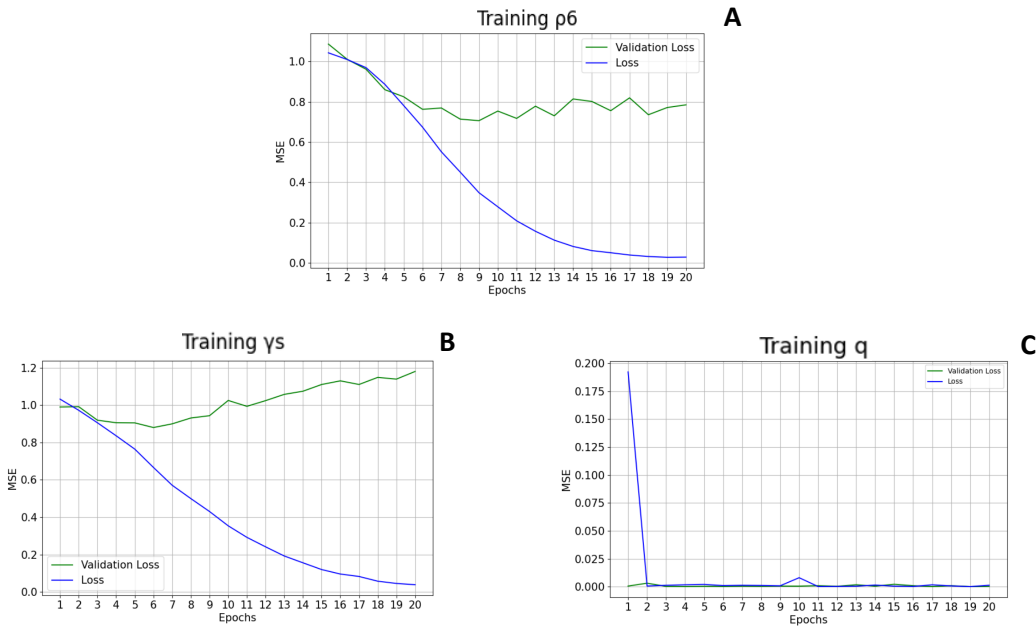


Figure 22: Training dynamics plots using  $\rho_6$  (A),  $\gamma_s$  (B) and  $q$  (C) as target variable. The training process was designed to retrieve the updated weights of the DM-CNN at the epoch corresponding to the lowest validation loss value.

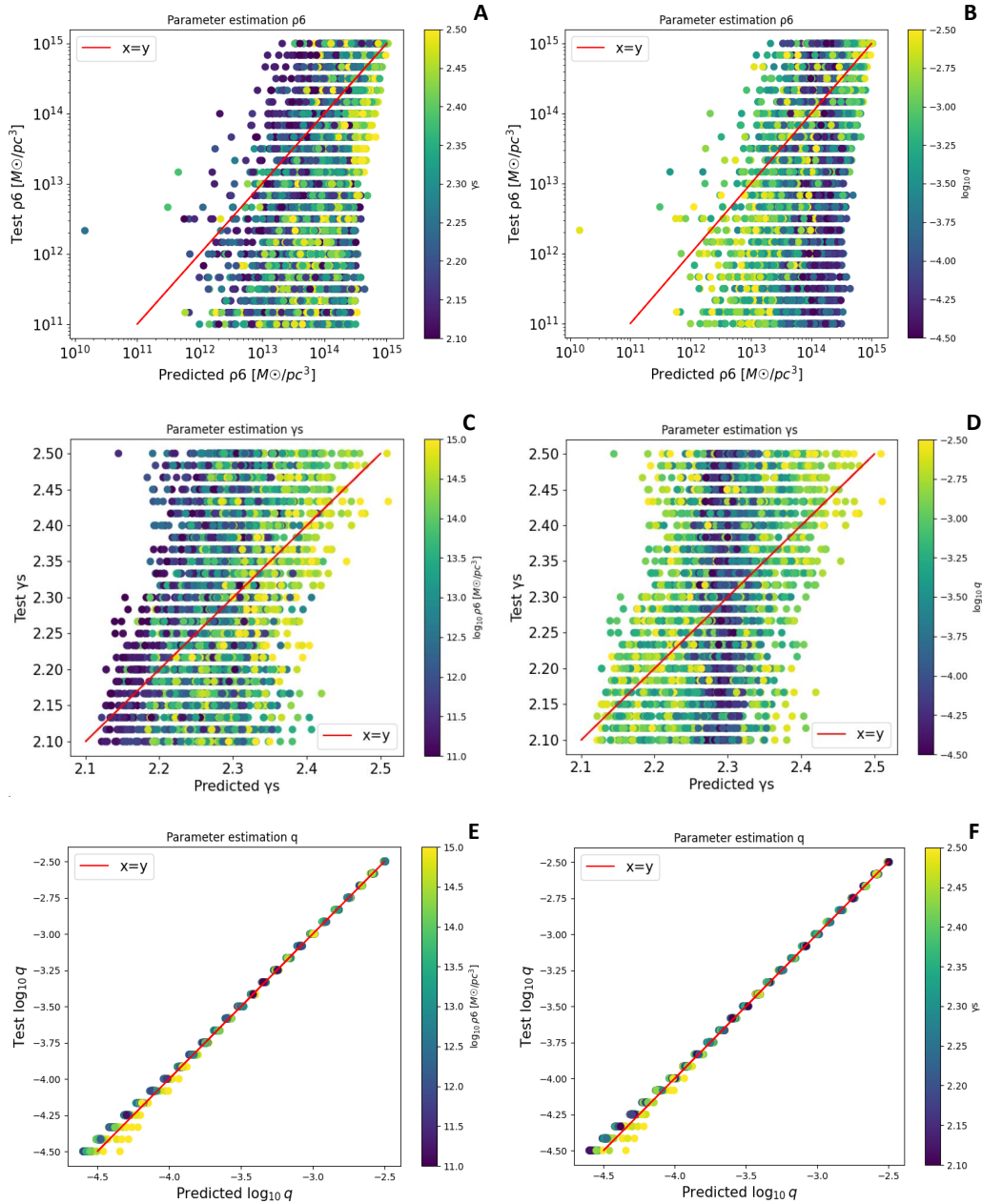


Figure 23: Plots of  $\rho_6$  (A and B),  $\gamma_s$  (C and D) and  $q$  (E and F) parameter estimation results. The colours of the scatter plots represents the parameters associated with the GW data which are not used as target variable during the training of the DM-CNN, as shown also in Fig. 20. Plots A and B are characterized with a bias in overestimating  $\rho_6$  target variable similarly displayed in the results associated with dataset 1.

The parameter prediction results generated from the application of the DM-CNN on the testing set are found in Fig. 23. The predictions of the  $\rho_6$  and  $\gamma_s$  test values are significantly less accurate and precise compared to the prediction of  $q$  test values. In fact, Fig. 23 E and Fig. 23

F show an almost perfect prediction of  $q$  test values independently of the associated  $\rho_6$  and  $\gamma_s$  values. The *Accuracy* of the DM-CNN for each bin of the parameters value range calculated on the testing set is displayed in Fig. 24.

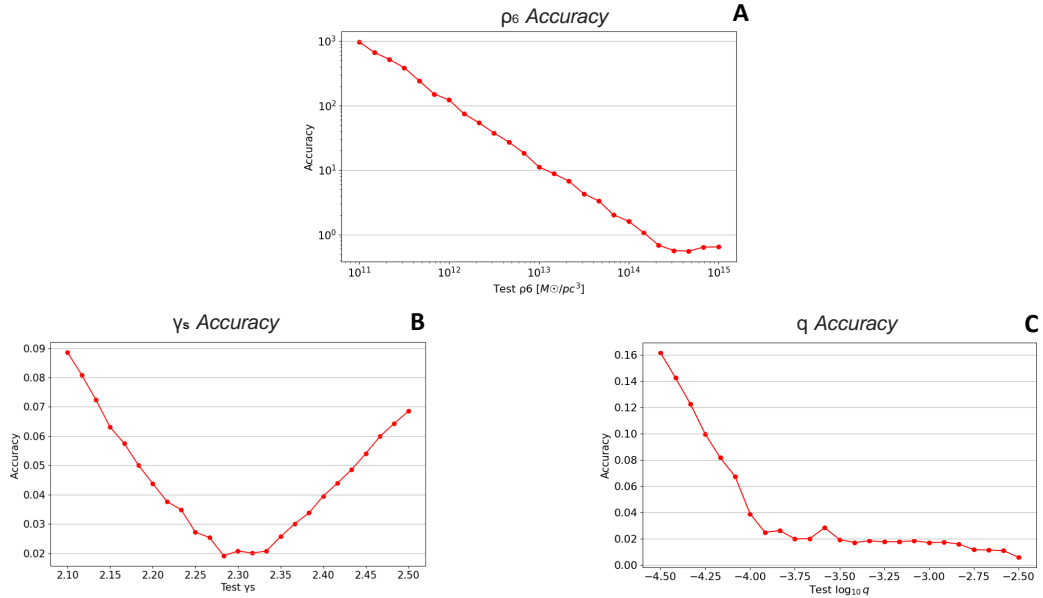


Figure 24: Accuracy plots associated with  $\rho_6$  (A),  $\gamma_s$  (B) and  $q$  (C) parameter estimation. Plot B shows a best  $\gamma_s$  prediction accuracy between 2.25 and 2.30 while plot C exhibits best  $q$  prediction accuracy above  $\log_{10}q = -4$ .

Fig. 24 A shows a potential region of best  $\rho_6$  parameter estimation between  $2 \times 10^{14}$  and  $4 \times 10^{14} M_\odot/pc^3$ . Fig. 24 B shows a significant range of  $\gamma_s$  parameter estimation from the application of the DM-CNN between 2.25 and 2.30. Finally, Fig. 24 C is consistent with the parameters prediction plots shown above, as the *Accuracy* of the DM-CNN rapidly improves until approximately  $\log_{10}q=-4$  and then stays constant. This indicates that the DM-CNN best estimates  $\log_{10}q$  target values in the range between -4 and -2.5. Furthermore, the  $R^2$  score is higher for the estimation of  $q$  parameter compared to the estimation of  $\rho_6$  and  $\gamma$  as shown in Table 6.

Metrics	$\rho_6$	$\gamma_s$	$q$
RMSE	2.03e14 [ $M_\odot/pc^3$ ]	0.11	1.31e-05
MAE	1.25e14 [ $M_\odot/pc^3$ ]	0.09	9.59e-06
$R^2$	30.0%	13.0%	100.0%

Table 6: Evaluation metrics computed for Dataset 2 on the entire parameter range.

Overall, by comparing the computed evaluation metrics across the two datasets (Table.5 and Table.6), a noticeable decrease of  $R^2$  score for the predicted  $\rho_6$  and  $\gamma_s$  parameter values can be seen (from 99.0% to 30.0% for  $\rho_6$  and from 72.0% to 11.0% for  $\gamma_s$ ). Moreover, the RMSE and MAE are higher for the estimation of  $\rho_6$  and  $\gamma_s$  in dataset 2 compared to dataset 1. This indicates that there was an overall decrease in the performance of the DM-CNN when expanding the GW

parameter analysis from 2 to 3 parameters. Previous work showed a parameter estimation result of  $\rho_6=1.7_{-0.6}^{+0.8} \times 10^{13} [M_\odot/pc^3]$ ,  $\gamma_s=2.2_{-0.05}^{+0.07}$ ,  $\log_{10}q=-3.1_{-0.3}^{+0.4}$  on a benchmark GW parameters system given by  $\rho_6=1.396 \times 10^{13} [M_\odot/pc^3]$ ,  $\gamma_s=2.25$  and  $\log_{10}(q)=-3.0$  (Cole et al., 2023). By extrapolating data from the *Accuracy* plots corresponding to the same parameters, the DM-CNN achieved a mean estimation of  $\rho_6=1.43 \pm 2.02 \times 10^{14} [M_\odot/pc^3]$  with  $\sigma=1.37 \times 10^{14} [M_\odot/pc^3]$ <sup>5</sup>,  $\gamma_s=2.33 \pm 0.07$  with  $\sigma=0.06$  and  $\log_{10}(q)=-2.998 \pm 0.006$  with  $\sigma=0.007$ , where the error bars represent the associated RMSE (Table 7). Therefore, with respect to a Bayesian approach, the DM-CNN had an overall worse  $\rho_6$  and  $\gamma_s$  parameter estimation when comparing the reference values estimation and taking into account the MAE on the whole  $\rho_6$  and  $\gamma_s$  parameter range indicated by larger errors in both cases. On the other hand, a better estimation of  $q$  target variables was achieved as indicated by a lower error in the estimation of the reference  $q$  value and of the total  $q$  test value range analyzed in this research project.

Parameter	DM-CNN	Bayesian inference
$\rho_6[M_\odot/pc^3]$	$1.43 \pm 2.02 \times 10^{14}$	$1.7_{-0.6}^{+0.8} \times 10^{13}$
$\gamma_s$	$2.33 \pm 0.07$	$2.2_{-0.05}^{+0.07}$
$\log_{10}(q)$	$-2.998 \pm 0.006$	$-3.1_{-0.3}^{+0.4}$

Table 7: Comparison with Bayesian inference results for single parameter value estimation. The error bars in the CNN application represent the RMSE while in the Bayesian inference results they represent the 68% credible intervals.

## 4 Discussion

The satisfactory parameter estimation performance obtained from the application of DM-CNN on the testing set of dataset 1 using  $\rho_6$  parameter as target variable can be explained by the fact that the GW signal dephasing is directly proportional to the value of  $\rho_{CMD}$  which in turn is dependent on  $\rho_6$ , as shown above in Equations (8) and (10). A higher  $\rho_6$  associated with DM spike will result in a higher loss of energy by the PBH binary system over time and in turn the phase of the GW will be more affected. This also explains why the proposed DL algorithm performs better in extracting dephased GW features from data exhibiting high  $\rho_6$  values. Moreover, the better performance in estimating  $\rho_6$  compared to  $\gamma_s$  can be attributed to a higher order range for  $\rho_6$  as shown in Table 1, which causes  $\rho_6$  to be the dominant DM spike parameter in the overall gravitational waveform. As explained above, the proposed initial value ranges allow to generate a phase difference with respect to vacuum of at least  $2\pi$  for all DM spike parameter combinations. This justifies the choice of setting the low end of the  $\rho_6$  value range at  $10^{11} M_\odot/pc^3$  rather than  $0 M_\odot/pc^3$  as done in previous work (Cole et al., 2023). Therefore, based on the initial assessment carried out on the dephasing effect for each DM spike parameter combination, the proposed DM-CNN was expected to successfully extract the dephased GW features in all waveforms with DM spike and correctly predict the associated DM parameters. However, the results show that this was not the case. One possible reason for the low prediction accuracy on GWs generated with  $\rho_6$  lower than approximately  $2 \times 10^{12} M_\odot/pc^3$  is the fact that most of the detector output is dominated by the simulated ET detector's noise as shown in Fig. 16, which potentially covers parts of the signal where the dephasing effect of less dense DM spike could show up. In fact,

<sup>5</sup>The standard deviation ( $\sigma$ ) measures the variability (or precision) of the predictions and it is calculated using the formula:  $\sigma = \sqrt{\frac{\sum_{i=1}^N (x_i - \bar{x})^2}{N}}$ , where  $N$  is the number of prediction,  $x_i$  represents each individual prediction and  $\bar{x}$  is the mean value of the predictions.

by using an additional preliminary dataset generated with a luminosity distance of 22.9 Mpc in which the simulated GW signal is above threshold and dominates the detector's output, the DM spike parameters estimation was found to be significantly higher throughout the entire arbitrary value ranges of both  $\rho_6$  and  $\gamma_s$  parameters. Therefore, the SNR of the GW signals played a crucial role in the prediction accuracy of the proposed DL algorithm.

The worse performance of the DM-CNN when applied on dataset 2 can be explained by the relatively high arbitrary value range of the  $q$  parameter used to generate the GW signals. Changing the mass ratio can drastically change the overall GW signal shape as the amplitude is directly proportional to the  $m_1$  and  $m_2$  values of the PBH binary system as shown in Equation (28). Therefore, a change in mass ratio has a significantly larger impact compared to a change in  $\rho_6$  or  $\gamma_s$ . This caused the DM parameter estimation to be significantly less efficient. The less accurate  $q$  parameter estimation exhibited for GW signals generated with  $\log_{10}(q) < -4$  can be explained by the fact that SNR is directly proportional to the chirp mass and  $m_1$  was kept constant while varying the mass ratio in dataset 2. As a result, GW signals with  $\log_{10}(q) > -3$  had an SNR of at least 12 which is considered to be the threshold of GW detectability in ET (Cole et al., 2023). Therefore, the mass ratio of the simulated PBH binaries had an impact on the prediction of the GW parameters.

In potential future work, several changes could be implemented in order to overcome some data and DL algorithm limitations that were encountered in this project. First of all, the data quality could be improved for instance by increasing the number of frequency bins over which the GW amplitude is generated. As a consequence, the generated GW signal shape would exhibit a higher resolution and the proposed DL algorithm would potentially extract features more efficiently and predict the DM spike parameters more accurately. Increasing the frequency bins of the dataset will, however, require more computational time to train the DM-CNN algorithm on larger data samples and additional modifications on the neural network architecture and hyperparameters would be required to accommodate for the larger data size. Moreover, increasing the number of data samples for each test bin by performing more data augmentation (e.g. from 40 random instances of ET noise to 100 for each DM spike parameter permutation of both datasets) could lead to enhanced fitting by the DM-CNN to the data and improved prediction. Furthermore, adding more test bins within the used parameter values ranges could be a useful modification in order to obtain a more in-depth understanding of the DM-CNN performance on finer changes of the DM spikes parameters. Finally, an additional dataset could be generated by assuming a DM dress consisting of an overdensity of several PBHs corresponding to a constant  $\gamma_s$  value equal to 2.25. This would allow to further simplify the parameter estimation problem even further and possibly achieve better accuracy on the  $\rho_6$  parameter prediction as found in previous work (Cole et al., 2023). Furthermore, Cole et al. (2023) also discovered that increasing the length of the GW signals from 1 week to 1 year improved the performance of Bayesian inference significantly as this allows to access more data about the PBH merger inspiral. Such modification could also be applied to both dataset 1 and 2 in order to enhance the parameter estimation performance of the DM-CNN in potential future research.

In regards of the proposed DL algorithm, a follow-up of this research would be performing a more exhaustive grid search over the space of hyperparameter values and experimenting with more complex CNN architectures or possibly other ML algorithms. Considering the proposed DM-CNN architecture, adding more convolution layers with smaller filter sizes (for instance 3x1 or 4x1) should theoretically lead to better feature extractions of the input data. As an alternative, consecutive convolution layers could be applied in order to develop more complex features of the input data before dropping some information using pooling. Adding dropout layers could improve parameter estimation by avoiding overfitting. Finally, other types of neural networks could have been investigated such as Long Short Term Memory (LSTM) networks (Hochreiter & Schmidhuber, 1997), which are a special type of Recurrent Neural Network. LSTMs use a more

generalized feedforward mechanism in order to transfer information between neurons since the output of one neuron depends not only on the activation function associated with that neuron but also on the computation made by the neuron on the previous layer. LSTMs are therefore optimal tools to model the sequence of data such that each sample is dependent on previous ones and is specifically targeted for times series. Therefore, the data could be converted into the time domain for LSTM application. This however would require sampling the signals at high frequencies in order to calculate the strain until the merger which would be computationally very heavy.

When it comes to the relevance of this research project to the GW astronomy community, different black hole mergers could be examined, such as supermassive black hole mergers using LISA sensitivities, to study the applicability of the DM-CNN for different orders of chirp masses. In addition, other intriguing environmental effects such as gravitational atoms and accretion disks on GW signals could be investigated in further research using the methods described in this manuscript. The potential results of this hypothetical research could provide new exciting insights for the study of DM and the possibility of developing a new tool used to differentiate between environmental effects.

## 5 Conclusion

In conclusion, the results from this master thesis project show that the DM-CNN model is suited for the parameter estimation of dephased GW signals in ET with a constant PBH binary mass ratio. The DM-CNN proposed here performed well when estimating GW signals parameters generated with  $\rho_6$  values between  $2 \times 10^{12}$ - $10^{15} M_\odot/pc^3$  in the scenario of a 2-parameter GW analysis. However, the DM-CNN was not successful in extracting DM parameters in the scenario of a 3-parameter GW analysis, but, on the other hand, it estimated correctly the PBH mergers mass ratio. Therefore, the results are partially in accordance with previous work in which the DM spike parameters associated with dressed PBH mergers were estimated with relatively low accuracy and precision on 7-day long GW data (Cole et al., 2023). The DM-CNN model must be considered as an initial prototype that has a lot of room for potential improvements as explained above. Therefore, based on the project's findings and discussion, the application of a more optimized version of the current DM-CNN architecture for the search of DM in 3G detectors in the future is very plausible.

## Acknowledgements

I would like to thank Prof. Dr. Christoph Weniger and Prof. Dr. Gianfranco Bertone for their supervision while conducting the master thesis research project. I would like to thank Dr. Philippa Cole from the Università degli Studi di Milano-Bicocca for the great help while using the pydd library for generating the dataset used throughout this research project. I would also like to thank Dr. Alessandro Parisi from the University of Amsterdam for his help in generating the dataset used for the initial approach aimed at performing the classification of GW signals with DM spike, which was not outlined in this master thesis.

## Appendix

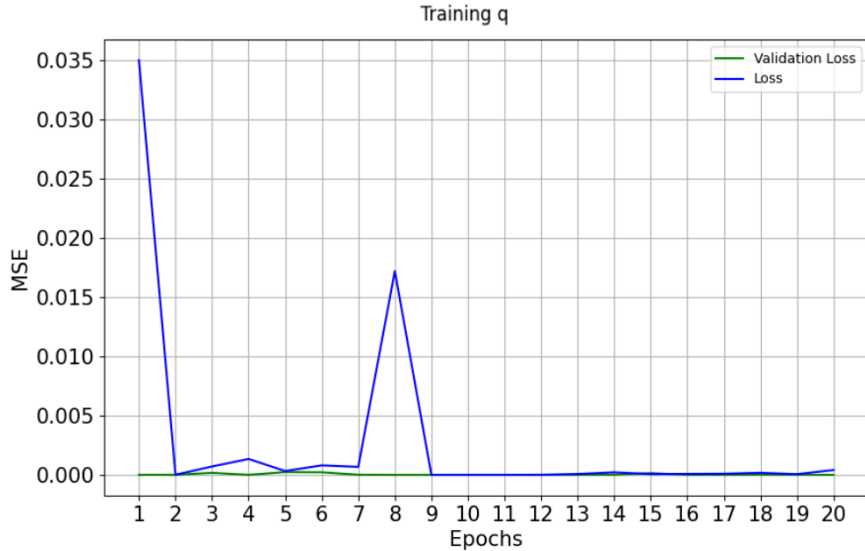


Figure 25: Training dynamics plot using  $q$  as target variable. The plot shows that the DM-CNN generalized well on unseen data denoted from the rapid drop of the validation loss to 0.

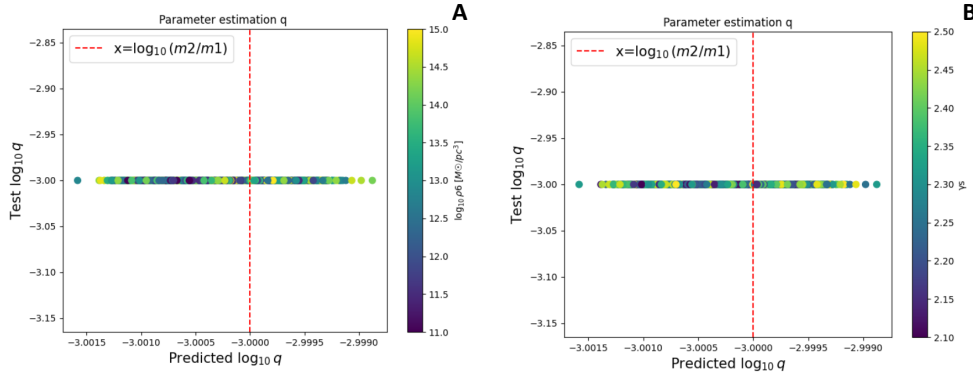


Figure 26: Plots of  $q$  (A and B) parameter estimation results. The graphs show a measured  $\log_{10}q = -3.0001 \pm 0.0010$ . The dotted vertical line represents the true  $q$  target value. The evaluation metrics table (Table 5) displays a MAE of  $1.09e-06$  and RMSE of  $1.38e-06$  indicating a higher performance in dataset 1 compared to dataset 2 in predicting  $q$  as target variable, as expected. The training dynamics plot and the evaluation metrics value indicate that the prediction of  $q$  as target variables was excellent in dataset 1. The colours of the scatter plot represent the associated  $\rho_6$  (A) and  $\gamma_s$  (B) values which were not used as target variables.

## References

- A., C., & B., K. (2021). *pydd*. <https://github.com/adam-coogan/pydd>. GitHub.
- Abbott, B. P., et al. (2009). LIGO: the laser interferometer gravitational-wave observatory. *Reports on Progress in Physics*, 72(7), 076901. Retrieved from <https://doi.org/10.1088%2F0034-4885%2F72%2F7%2F076901> doi: 10.1088/0034-4885/72/7/076901
- Abbott, B. P., et al. (2016). Observation of Gravitational Waves from a Binary Black Hole Merger. *Phys. Rev. Lett.*, 116, 061102. Retrieved from <https://link.aps.org/doi/10.1103/PhysRevLett.116.061102>
- Abbott, B. P., et al. (2017a). Gravitational waves and gamma-rays from a binary neutron star merger: GW170817 and GRB 170817a. *The Astrophysical Journal*, 848(2), L13. doi: 10.3847/2041-8213/aa920c
- Abbott, B. P., et al. (2017b). GW170817: Observation of Gravitational Waves from a Binary Neutron Star Inspiral. *Phys. Rev. Lett.*, 119, 161101. Retrieved from <https://link.aps.org/doi/10.1103/PhysRevLett.119.161101>
- Abbott, B. P., et al. (2018). Prospects for observing and localizing gravitational-wave transients with Advanced LIGO, Advanced Virgo and KAGRA. *Living Reviews in Relativity*, 21(1), 3. Retrieved from <https://doi.org/10.1007/s41114-018-0012-9>
- Abernathy, M., et al. (2011). Einstein gravitational wave Telescope conceptual design study. Retrieved from <http://www.et-gw.eu/index.php/etdsdocument>
- Affeldt, C., et al. (2014). Advanced techniques in GEO 600. *Classical and Quantum Gravity*, 31(22), 224002. Retrieved from <https://doi.org/10.1088%2F0264-9381%2F31%2F22%2F224002> doi: 10.1088/0264-9381/31/22/224002
- Amaro-Seoane, P., Audley, H., Babak, S., Baker, J., Barausse, E., Bender, P., ... Zweifel, P. (2017). *Laser interferometer space antenna*.
- Aprile, E., Aalbers, J., Agostini, F., Alfonsi, M., Althueser, L., Amaro, F., ... Zopounidis, J. (2020, nov). Projected WIMP sensitivity of the XENONnT dark matter experiment. *Journal of Cosmology and Astroparticle Physics*, 2020(11), 031–031. Retrieved from <https://doi.org/10.1088%2F1475-7516%2F2020%2F11%2F031> doi: 10.1088/1475-7516/2020/11/031
- Babak, S., Balasubramanian, R., Churches, D., Cokelaer, T., & Sathyaprakash, B. S. (2006). A template bank to search for gravitational waves from inspiralling compact binaries: I. physical models. *Classical and Quantum Gravity*, 23(18), 5477–5504. Retrieved from <http://dx.doi.org/10.1088/0264-9381/23/18/002> doi: 10.1088/0264-9381/23/18/002
- Barack, L., Cardoso, V., Nissanke, S., Sotiriou, T. P., Askar, A., Belczynski, C., ... Zilhão, M. (2019, jun). Black holes, gravitational waves and fundamental physics: a roadmap. *Classical and Quantum Gravity*, 36(14), 143001. Retrieved from <https://doi.org/10.1088%2F1361-6382%2Fab0587> doi: 10.1088/1361-6382/ab0587
- Baumann, D., Bertone, G., Stout, J., & Tomaselli, G. M. (2022, Jun). Sharp signals of boson clouds in black hole binary inspirals. *Phys. Rev. Lett.*, 128, 221102. Retrieved from <https://link.aps.org/doi/10.1103/PhysRevLett.128.221102> doi: 10.1103/PhysRevLett.128.221102

- Bengio, Y. (2012). Practical recommendations for gradient-based training of deep architectures. *CoRR, abs/1206.5533*. Retrieved from <http://arxiv.org/abs/1206.5533>
- Bergstra, J., & Bengio, Y. (2012). Random search for hyper-parameter optimization. *The Journal of Machine Learning Research, 13*, 281-305.
- Bernabei, R., Belli, P., Cappella, F., Cerulli, R., Dai, C. J., d'Angelo, A., ... Ye, Z. P. (2010, mar). New results from DAMA/LIBRA. *The European Physical Journal C, 67(1-2)*, 39–49. Retrieved from <https://doi.org/10.1140/2Fepjc%2Fs10052-010-1303-9> doi: 10.1140/epjc/s10052-010-1303-9
- Billard, J., Figueroa-Feliciano, E., & Strigari, L. (2014, jan). Implication of neutrino backgrounds on the reach of next generation dark matter direct detection experiments. *Physical Review D, 89(2)*. Retrieved from <https://doi.org/10.1103%2Fphysrevd.89.023524> doi: 10.1103/physrevd.89.023524
- Caron, B., et al. (1997). The virgo interferometer for gravitational wave detection. *Nuclear Physics B - Proceedings Supplements, 54(3)*, 167 - 175. Retrieved from <http://www.sciencedirect.com/science/article/pii/S0920563297001096> doi: [https://doi.org/10.1016/S0920-5632\(97\)00109-6](https://doi.org/10.1016/S0920-5632(97)00109-6)
- Carr, B., Kohri, K., Sendouda, Y., & Yokoyama, J. (2021, November). Constraints on primordial black holes. *Reports on Progress in Physics, 84(11)*, 116902. Retrieved from <http://dx.doi.org/10.1088/1361-6633/ac1e31> doi: 10.1088/1361-6633/ac1e31
- Carroll, S. M. (2004). *Spacetime and geometry*. Pearson/Addison Wesley.
- Chandrasekhar, S. (1943, March). Dynamical Friction. I. General Considerations: the Coefficient of Dynamical Friction. , 97, 255. doi: 10.1086/144517
- Chayan Chatterjee, K. V. M. K., Linqing Wen, & Datta, A. (2019). *Using deep learning to localize gravitational wave sources*. Retrieved from <https://arxiv.org/abs/1909.06367>
- Cholis, I., Finkbeiner, D. P., Goodenough, L., & Weiner, N. (2009, December). The pamela positron excess from annihilations into a light boson. *Journal of Cosmology and Astroparticle Physics, 2009(12)*, 007–007. Retrieved from <http://dx.doi.org/10.1088/1475-7516/2009/12/007> doi: 10.1088/1475-7516/2009/12/007
- Chollet, F., et al. (2015). *Keras*. <https://keras.io>.
- Cole, P. S., Bertone, G., Coogan, A., Gaggero, D., Karydas, T., Kavanagh, B. J., ... Tomaselli, G. M. (2022). *Disks, spikes, and clouds: distinguishing environmental effects on bbh gravitational waveforms*.
- Cole, P. S., Coogan, A., Kavanagh, B. J., & Bertone, G. (2023, apr). Measuring dark matter spikes around primordial black holes with einstein telescope and cosmic explorer. *Physical Review D, 107(8)*. Retrieved from <https://doi.org/10.1103%2Fphysrevd.107.083006> doi: 10.1103/physrevd.107.083006
- Craig, N., & Katz, A. (2015, oct). The fraternal WIMP miracle. *Journal of Cosmology and Astroparticle Physics, 2015(10)*, 054–054. Retrieved from <https://doi.org/10.1088%2F1475-7516%2F2015%2F10%2F054> doi: 10.1088/1475-7516/2015/10/054
- de Swart, J. G., Bertone, G., & van Dongen, J. (2017, mar). How dark matter came to matter. *Nature Astronomy, 1(3)*. Retrieved from <https://doi.org/10.1038%2Fs41550-017-0059> doi: 10.1038/s41550-017-0059

- Einstein, A. (1918). *Über Gravitationswellen*. Annalen der Physik.
- European Space Agency. (2019). *The LISA spacecraft constellation*. Retrieved from <https://sci.esa.int/web/lisa/-/46429-the-lisa-spacecraft-constellation>
- Event Horizon Telescope Collaboration, Akiyama, K., Alberdi, A., & et al. (2019, April). First M87 Event Horizon Telescope Results. I. The Shadow of the Supermassive Black Hole. , 875, L1. Retrieved from <https://doi.org/10.3847/2041-8213/ab0ec7> doi: 10.3847/2041-8213/ab0ec7
- Ezquiaga, J. M., & Zumalacarregui, M. (2018, 12). Dark energy in light of multi-messenger gravitational-wave astronomy. *Frontiers in Astronomy and Space Sciences*, 5. doi: 10.3389/fspas.2018.00044
- George, D., & Huerta, E. (2018). Deep Learning for real-time gravitational wave detection and parameter estimation: Results with Advanced LIGO data. *Physics Letters B*, 778, 64 - 70. Retrieved from <http://www.sciencedirect.com/science/article/pii/S0370269317310390>
- Goodfellow, I., Bengio, Y., & Courville, A. (2016). *Deep learning*. MIT Press.
- Gravitational Wave International Committee. (2019). *The Next-Generation Global Gravitational-Wave Observatory New Astrophysics with the Farthest, Oldest, and Most Violent Events in the Universe*. Retrieved 2019-09-16, from <https://gwic.ligo.org/3Gsubcomm/documents/science-case.pdf>
- Hild, S., Abernathy, M., Acernese, F., Amaro-Seoane, P., Andersson, N., Arun, K., ... Yamamoto, K. (2011, apr). Sensitivity studies for third-generation gravitational wave observatories. *Classical and Quantum Gravity*, 28(9), 094013. Retrieved from <https://dx.doi.org/10.1088/0264-9381/28/9/094013> doi: 10.1088/0264-9381/28/9/094013
- Hirata, C. M. (2011, May). Lindblad resonance torques in relativistic discs - i. basic equations: Lindblad resonances - i. *Monthly Notices of the Royal Astronomical Society*, 414(4), 3198–3211. Retrieved from <http://dx.doi.org/10.1111/j.1365-2966.2011.18617.x> doi: 10.1111/j.1365-2966.2011.18617.x
- Hochreiter, S., & Schmidhuber, J. (1997). Long short-term memory. *Neural computation*, 9, 1735-80. doi: 10.1162/neco.1997.9.8.1735
- Hodson, T. O. (2022). Root-mean-square error (rmse) or mean absolute error (mae): when to use them or not. *Geoscientific Model Development*, 15(14), 5481–5487. Retrieved from <https://gmd.copernicus.org/articles/15/5481/2022/> doi: 10.5194/gmd-15-5481-2022
- Iglesias, G., Talavera, E., González-Prieto, , Mozo, A., & Gómez-Canaval, S. (2023, March). Data augmentation techniques in time series domain: a survey and taxonomy. *Neural Computing and Applications*, 35(14), 10123–10145. Retrieved from <http://dx.doi.org/10.1007/s00521-023-08459-3> doi: 10.1007/s00521-023-08459-3
- Jin, L., Li, S., Yu, J., & He, J. (2018). Robot manipulator control using neural networks: A survey. *Neurocomputing*, 285, 23–34. Retrieved 2019-03-25, from <http://www.sciencedirect.com/science/article/pii/S0925231218300158> doi: 10.1016/j.neucom.2018.01.002
- Kavanagh, B. J. (2020, February). *bradkav/halofeedback: Pre-release version*. Zenodo. Retrieved from <https://doi.org/10.5281/zenodo.3688813> doi: 10.5281/zenodo.3688813

- Kavanagh, B. J., Nichols, D. A., Bertone, G., & Gaggero, D. (2020, October). Detecting dark matter around black holes with gravitational waves: Effects of dark-matter dynamics on the gravitational waveform. *Physical Review D*, 102(8). Retrieved from <http://dx.doi.org/10.1103/PhysRevD.102.083006> doi: 10.1103/physrevd.102.083006
- Kingma, D., & Ba, J. (2014). Adam: A method for stochastic optimization. *International Conference on Learning Representations*.
- Kohavi, R. (1995). A study of cross-validation and bootstrap for accuracy estimation and model selection. In *Proceedings of the 14th international joint conference on artificial intelligence (ijcai)* (Vol. 2, pp. 1137–1143).
- Kuchibhotla, A. K., Brown, L. D., Buja, A., & Cai, J. (2019). *All of linear regression*.
- LIGO Scientific Collaboration. (2019). *The science of LSC research*. Retrieved 2019-09-16, from <https://www.ligo.org/science/GW-Sources.php>
- Milgrom, M. (1983, July). A modification of the Newtonian dynamics as a possible alternative to the hidden mass hypothesis. , 270, 365-370. doi: 10.1086/161130
- Nielsen, M. (2015). *Neural networks and deep learning*. Determination Press. Retrieved from <http://neuralnetworksanddeeplearning.com>
- Patterson, J., & Gibson, A. (2017). *Deep Learning: A Practitioner's Approach* (1st ed.). O'Reilly Media, Inc.
- Pedregosa, F., Varoquaux, G., Gramfort, A., Michel, V., Thirion, B., Grisel, O., ... Duchesnay, E. (2011). Scikit-learn: Machine learning in Python. *Journal of Machine Learning Research*, 12, 2825–2830.
- Peebles, P. J. E. (1993). *Principles of physical cosmology*. Princeton University Press.
- Razzano, M., & Cuoco, E. (2018). Image-based deep learning for classification of noise transients in gravitational wave detectors. *Classical and Quantum Gravity*, 35(9), 095016. Retrieved from <http://dx.doi.org/10.1088/1361-6382/aab793> doi: 10.1088/1361-6382/aab793
- Robert, C. P., Marin, J.-M., & Rousseau, J. (2010). *Bayesian inference*.
- Roy, S. K., Mukhopadhyay, S., Lahiri, J., Atta, D., Chowdhury, P. R., & Basu, D. (2020, April). Gravitational waves from non-radial perturbations in neutron stars. *Annals of Physics*, 415, 168121. Retrieved from <http://dx.doi.org/10.1016/j.aop.2020.168121> doi: 10.1016/j.aop.2020.168121
- Saha, S. (2018). *A comprehensive guide to convolutional neural networks — the eli5 way*. Retrieved 2019-27-12, from <https://towardsdatascience.com/a-comprehensive-guide-to-convolutional-neural-networks-the-eli5-way-3bd2b1164a53>
- Sharma, S. (2017, August). Markov chain monte carlo methods for bayesian data analysis in astronomy. *Annual Review of Astronomy and Astrophysics*, 55(1), 213–259. Retrieved from <http://dx.doi.org/10.1146/annurev-astro-082214-122339> doi: 10.1146/annurev-astro-082214-122339
- Shen, H., George, D., Huerta, E. A., & Zhao, Z. (2017). *Denoising gravitational waves using deep learning with recurrent denoising autoencoders*. Retrieved from <https://arxiv.org/abs/1711.09919>

- Sofue, Y. (2020). *Rotation curve of the milky way and the dark matter density*. arXiv. Retrieved from <https://arxiv.org/abs/2004.11688> doi: 10.48550/ARXIV.2004.11688
- SURF. (2024). *Snellius: The National Supercomputer*. Retrieved from <https://www.surf.nl/en/services/snellius-the-national-supercomputer> (Accessed: January 18, 2024)
- Usman, S. A., et al. (2016). The PyCBC search for gravitational waves from compact binary coalescence. *Class. Quant. Grav.*, 33(21), 215004. doi: 10.1088/0264-9381/33/21/215004
- Vicente, R., Cardoso, V., & Lopes, J. C. (2018, April). Penrose process, superradiance, and ergoregion instabilities. *Physical Review D*, 97(8). Retrieved from <http://dx.doi.org/10.1103/PhysRevD.97.084032> doi: 10.1103/physrevd.97.084032
- Weisberg, J. M., Nice, D. J., & Taylor, J. H. (2010). Timing Measurements of the Relativistic Binary Pulsar PSR B1913+16. *The Astrophysical Journal*, 722(2), 1030-1034. doi: 10.1088/0004-637X/722/2/1030
- Willke, B., et al. (2002). The GEO 600 gravitational wave detector. *Classical and Quantum Gravity*, 19(7), 1377–1387. Retrieved from <https://doi.org/10.1088%2F0264-9381%2F19%2F7%2F321> doi: 10.1088/0264-9381/19/7/321
- Yalçın, O. G. (2018). *Image classification in 10 minutes with mnist dataset*. Retrieved 2019-11-12, from <https://towardsdatascience.com/image-classification-in-10-minutes-with-mnist-dataset-54c35b77a38d>
- Yamada, K., & Inaba, S. (2010, October). Type i migration in radiatively efficient discs: Type i migration in radiatively efficient discs. *Monthly Notices of the Royal Astronomical Society*, 411(1), 184–192. Retrieved from <http://dx.doi.org/10.1111/j.1365-2966.2010.17670.x> doi: 10.1111/j.1365-2966.2010.17670.x